Probing the Standard Model: Preparation of a new Electron Asymmetry Measurement in the Decay of Polarized Neutrons

This diploma thesis has been carried out by
Marc Schumann
at the Physics Institute of the University Heidelberg
unter the supervision of
Priv.-Doz. Dr. Hartmut Abele.

January 2004

Abstract

Probing the Standard Model: Preparation of a new Electron Asymmetry Measurement in the Decay of Polarized Neutrons

We report on preparations for a new precision measurement of the electron asymmetry A. This correlation between neutron spin and electron momentum will be obtained in the decay of free polarized neutrons using the electron spectrometer *PERKEO II* in a new setup. Compared to the last A-measurement with this instrument we improve the setup at several points: We can reduce the background from the collimation system by 90 % without losing much count rate. By changing the data acquisition system to VME we were able to decrease its dead time dramatically.

Furthermore, we present measurements on the detector function and the results of the first part of the beamtime, which was performed at the Institut Laue-Langevin (ILL) in Grenoble (France). There we managed to produce the best polarized cold neutrons beam so far, with an average polarization of $P = 99.7$ % for wavelengths between 2 and 12 Å.

Zusammenfassung

Ein Test des Standardmodells: Vorbereitung einer neuen Messung der Elektronen-Asymmetrie im Zerfall polarisierter Neutronen

Wir berichten über die Vorbereitungen eines neuen Präzisionsexperiments zur Messung der Elektronen-Asymmetrie A. Diese Korrelation zwischen Neutronenspin und Elektronenimpuls soll im Zerfall polarisierter, freier Neutronen mit dem Spektrometer *PERKEO II* bestimmt werden. Im Vergleich zur letzten A-Messung verbessern wir den Aufbau des Experiments an verschiedenen Stellen: Wir können den Untergrund, der im Kollimationssystem entsteht, um etwa 90 % verringern, ohne dabei signifikant an Zählrate zu verlieren. Indem wir das Datennahmesystem auf VME umgestellt haben, konnten wir seine Totzeit drastisch verringern.

Weiterhin präsentieren wir Messungen zur Bestimmung der Detektorfunktion und die Ergebnisse der ersten Strahlzeit, welche am Institut Laue-Langevin (ILL) in Grenoble (Frankreich) durchgeführt wurde. Uns ist es dabei gelungen, den bislang best-polarisierten Strahl kalter Neutronen herzustellen, welcher eine mittlere Polarisation von P= 99.7 % in einem Wellenlängenbereich von 2 bis 12 Å aufweist.

This thesis is dedicated to everyone who has supported me on my way through the world of physics.

Contents

Chapter 1

Introduction

More than 30 years ago the standard model of particle physics, which describes the phenomena of electroweak and strong interaction, was completed in its basics. Whenever a new effect was discovered (e.g. the third quark generation), it was just added to this gauge theory. Because of this, physicists are more and more surprised that the standard model is still valid. Even the non-zero neutrino masses can be inserted without bigger problems but with more and more effects included the number of free parameters grows: There are 18 parameters in the "old" standard model and another seven must be added to account for massive neutrinos. So most scientists think that the standard model of particle physics cannot be the most basic theory and are looking for hints on "physics beyond the standard model".

PERKEO II, the topic of this thesis, is a high precision experiment to test the standard model and to search for "new physics". It measures the electron asymmetry A in neutron decay, that means the spatial anisotropy in the emission of the electrons. Hence *PERKEO II* can be seen as a modern version of the Wu experiment, which discovered parity violation in 1957 [Wu57]. But instead of using ^{60}Co nuclei, we examine the β-decay of the free polarized neutron, which is a much simpler system.

With a precise measurement of the asymmetry A, one can perform a test on the unitarity of the quark mixing CKM-matrix. A deviation of 3 standard deviations σ from unitarity was published by the *PERKEO II* group in 2002 [Abe02].[1] The next run of the experiment should reach even higher precision. This is the main subject of this thesis: To increase the precision at several points.

This can be achieved by background reduction (chapter 3) and by optimizing the detector system (chapter 4). Since we have changed the data acquisition system from CAMAC to VME, we managed to reduce the dead time dramatically, which is presented in chapter 5. In chapter 6, we summarize the results of the first part of the beamtime at the Institut Laue-Langevin (ILL) in fall 2003. There we achieved a beam polarization of 99.7 %, which is again a big step towards higher precision. To begin with, we give a short introduction to the theory and the experimental setup of the spectrometer *PERKEO II*.

[1] Due to a sign error in a theoretical correction found in 2002 the deviation reduced to 2.7σ [Mar03].

Chapter 2

PERKEO Overview

In this chapter we give a brief introduction to the theory of weak interactions since the neutron decay can be seen as the prototype process for semileptonic weak decays. In the second part, we present the spectrometer *PERKEO II* and how we get from the measured angular correlation coefficient A, the correlation between neutron-spin and electron-momentum, to the theoretical parameters of the standard model.

2.1 Theory

2.1.1 The Neutron and the Neutron Decay

The neutron with the mass of $m_n = 939.565$ MeV c^{-2} (all data taken from [PDG02]) is the heavier particle of the two nucleons. If it is not bound in a nucleus, it decays with a mean lifetime $\tau = (886 \pm 1)$ s into a proton, an electron and an anti-neutrino:

$$n \rightarrow p + e^- + \overline{\nu}_e. \tag{2.1}$$

Since the neutron decays into three particles, the process has a continuous spectrum (see figure 2.1). The q-value of the decay is

$$q = (m_n - m_p - m_e - m_\nu)\, c^2 = 782.32 \text{ keV}. \tag{2.2}$$

If we consider the proton recoil energy (and neglect the neutrino), we get an endpoint energy of $E_0 = 781.57$ keV.

Uncorrected Spectrum: The decay probability ω depends on the kinetic energy E of the electron and is given by Fermi's "Golden Rule" (see e.g. [Pov01])

$$\mathrm{d}\omega(E) = \frac{2\pi}{\hbar}\, |T_{if}|^2\, \frac{\mathrm{d}\phi(E)}{\mathrm{d}E}\, \mathrm{d}E, \tag{2.3}$$

where T_{if} is the transition matrix element that will be discussed in chapter 2.1.2. The number of possible final states is given by the phase space factor

$$\mathrm{d}\phi(E) = \frac{V^2}{4\pi^4(\hbar c)^6}\,(E + m_e c^2)\,\sqrt{(E + m_e c^2)^2 - m_e^2 c^4}\,(E_0 - E)^2\,\mathrm{d}E = f(E)\,\mathrm{d}E. \quad (2.4)$$

V^2 is the normalizing volume. It cancels since it also appears in the matrix element, so that the decay probability is independent of this volume.

The shape of the spectrum, which is solely determined by the phase space factor, is shown in figure 2.1.

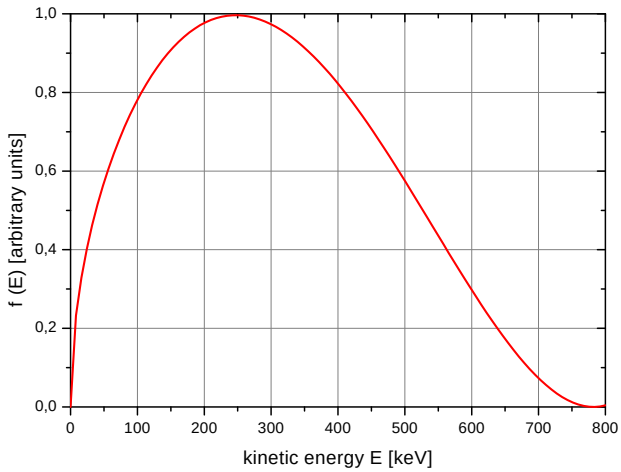

Figure 2.1: The phase space factor $f(E)$ of the β-spectrum without corrections.

Corrections: Since there is an attractive force between proton and electron, we have to account for a small Coulomb correction, which is given by the Fermi-Function[1]

$$F(E) = \frac{2\pi\eta}{1 - \exp(-2\pi\eta)}\,, \qquad \text{with} \quad \eta = \frac{\alpha}{\beta}\,,\ \alpha = \frac{e^2}{\hbar c}\,,\ \beta = \frac{v}{c}. \quad (2.5)$$

Additionally, the spectrum has to be corrected due to outer radiative corrections $\delta_R(E)$ and due to proton recoil $R_0(E)$, so that the phase space factor now reads

$$f^*(E) = f(E)\,\Big(1 + \delta_R(E)\Big)\,\Big(1 + R_0(E)\Big)\,F(E). \quad (2.6)$$

Parity Violation in β-Decay: In 1957, Wu showed experimentally that parity is not conserved in weak interactions [Wu57]. Parity is maximally violated, that means that the coefficients of the vector and the axial-vector part of the matrix element have the same

[1] The Fermi function is a classical approximation better than $5 \cdot 10^{-4}$ for $E > 5$ keV [Bae96].

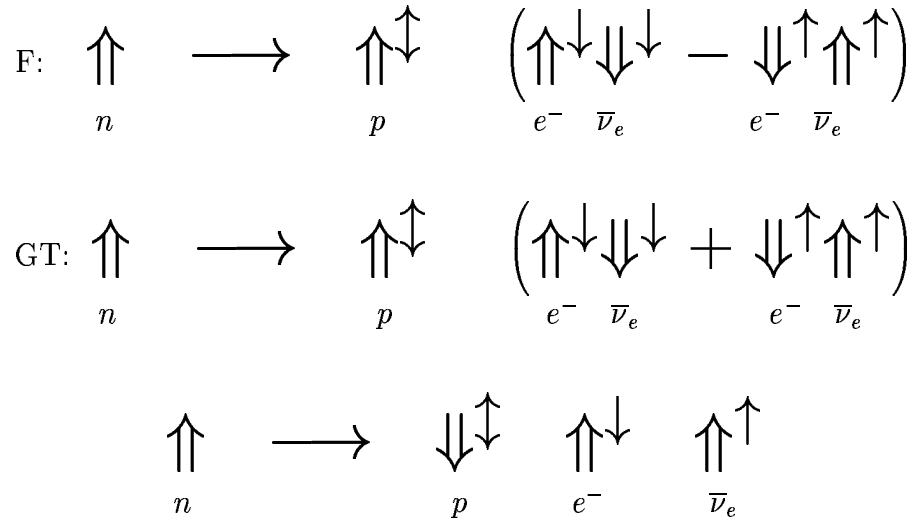

Figure 2.2: Fermi- (F) and Gamow-Teller transitions (GT). The double arrows represent the spin, the superscript arrow the momentum. Only the transition on the bottom is parity violating because the electron has to have the momentum anti-parallel to the neutron spin (in the limit $v = c$) due to angular momentum conservation. (Figure based on [Rei99].)

strength and opposite signs. Because of this the theory is called V-A-interaction ("vector minus axialvector"). This implies that the (massless) neutrinos are always left-handed[2] whereas anti-neutrinos are always right-handed. The charged leptons created in weak interactions are also left-handed, but their spin is only aligned with a polarization degree of $\beta = \frac{v}{c}$.

There are two possible transitions in the β-decay: The transition via the vector coupling is called Fermi-transition. It conserves the spin orientation of the hadrons. As we can see in figure 2.2, the emission of the decay particles is isotropic and parity is conserved.

The hadron spin can be flipped in one of the two axial-vector transitions (Gamow-Teller). Then the spin of the anti-neutrino has to be aligned with its momentum since it is always right-handed (if it has a finite mass, it is almost right-handed). Hence the electron is emitted preferredly against its spin due to momentum conservation, the emission is anisotropic and parity is violated in this Gamow-Teller transition (see figure 2.2, bottom).

[2]The left- and right-handed part of a particle field ψ is defined by $\psi_{\substack{L\\R}} = \frac{1\mp\gamma^5}{2}\,\psi$, $\overline{\psi}_{\substack{L\\R}} = \overline{\psi}\,\frac{1\pm\gamma^5}{2}$. ($\gamma^5 = i\gamma^0\gamma^1\gamma^2\gamma^3 = \left(\begin{smallmatrix}0 & \mathbf{1}\\ \mathbf{1} & 0\end{smallmatrix}\right)$). The transformation $\psi' = -\gamma^5\psi$ is called chiral transformation and $\psi_{\substack{L\\R}}$ are its eigenstates with eigenvalues ∓ 1.

2.1.2 Weak Interaction and CKM-Matrix

On the quark level, the neutron decay can be regarded as a transition from a down- to an up-quark as it is shown in figure 2.3. But since the gauge-field, the W-boson, has the very large mass of $m_W = (80.4 \pm 0.4)$ GeV c^{-2} [PDG02], it dominates the propagator against the momentum transfer q, which is very small in β-decay:

$$\frac{1}{q^2c^2 + m_W^2c^4} \xrightarrow{q\approx 0} \frac{1}{m_W^2c^4} = \text{const.} \tag{2.7}$$

Therefore the propagator and the couplings to the leptons can be written as a constant: The Fermi-constant $G_F = 1.16 \cdot 10^{-5}$ GeV^{-2} $(\hbar c)^{-3}$ [PDG02].

Historically, before the gauge theories came up, Fermi postulated a simple current-current interaction, analogous to the electromagnetic interaction, to describe the β-decay:

$$\mathcal{L} = G_F \ (\overline{p}\gamma^\mu n) \ (\overline{e}\gamma_\mu \nu_e) + h.c. \tag{2.8}$$

(The letters for the particles (n,ν_e) represent Dirac spinors and $\overline{p} = p^\dagger\gamma^0$, $\overline{e}$ are adjoint spinors.) This model works quite well for low energetic processes, but it is not renormalizable and cannot describe parity violation.

Parity Violation and V-A-Theory: To account for parity violation, the interaction has to have vector and axial-vector contributions with coefficients c_V and c_A. Experiments show that parity is maximally violated ($|c_V| = |c_A|$) and the interaction only couples to left-handed fermions and right-handed anti-fermions, i.e. $c_V = -c_A = 1$. Therefore the projection operator $\frac{1}{2}(1 - \gamma^5)$ is used in the Lagrangian of the V-A-theory to include this result:

$$\mathcal{L} = -\frac{G_F}{\sqrt{2}} \left(\overline{p}\gamma^\mu \left(1 + \frac{g_A}{g_V}\gamma^5\right) n\right) \left(\overline{e}\gamma_\mu(1 - \gamma^5)\nu_e\right) + h.c. \tag{2.9}$$

On the quark level, parity is also violated maximally; for baryons there is in fact no deviatition from the V-A-structure, but the strength of the hadronic current is changed by two constants, g_V and g_A, that differ from the leptonic case.

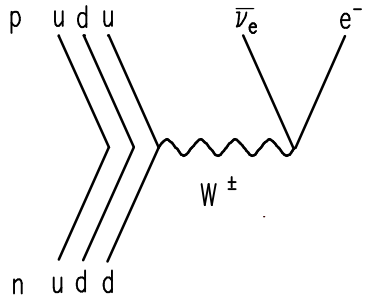

Figure 2.3: Feynman diagram of the neutron β-decay.

Quark-Mixing: Within the standard model, parity violation is achieved by introducing left-handed SU(2) doublets,

$$\begin{pmatrix} \nu_e \\ e_L \end{pmatrix}, \quad \begin{pmatrix} \nu_\mu \\ \mu_L \end{pmatrix}, \quad \begin{pmatrix} \nu_\tau \\ \tau_L \end{pmatrix}, \quad \text{and} \quad \begin{pmatrix} u_L \\ d_L \end{pmatrix}. \tag{2.10}$$

The right handed particles are singlets under SU(2) transformation so they do not interact weakly at all. Every leptonic weak process can be described using one coupling constant, what is called "universality of the weak interaction".

A particle can change into its doublet partner emitting a W^--boson. But there are also processes, coupling the first to the second (third) quark generation, what cannot be explained in this simple doublet picture. To include also strangness violating decays like

$$\Lambda\ (sud) \rightarrow p\ (uud) + e + \overline{\nu_e}, \tag{2.11}$$

and preserve universality, the quark field d must be replaced by a linear combination of d, s and b fields:

$$d \rightarrow d' = V_{ud}\ d + V_{us}\ s + V_{ub}\ b. \tag{2.12}$$

That means, that the mass basis (d) of the quarks is not identical with the basis of the weak interaction (d') and the left-handed quark doublet now reads

$$\begin{pmatrix} u_L \\ d'_L \end{pmatrix}. \tag{2.13}$$

Of course, this is the case for all three quark generations and the transformation between the two bases is done by an unitary 3×3 matrix V:

$$\begin{pmatrix} d' \\ s' \\ b' \end{pmatrix} = \begin{pmatrix} V_{ud} & V_{us} & V_{ub} \\ V_{cd} & V_{cs} & V_{cb} \\ V_{td} & V_{ts} & V_{tb} \end{pmatrix} \begin{pmatrix} d \\ s \\ b \end{pmatrix}. \tag{2.14}$$

It is called the Cabibbo-Kobayashi-Maskawa- or CKM-matrix

The β-Decay Matrix Element: We can use the neutron decay to determine V_{ud}. The matrix element for the process reads

$$T_{if} = -\frac{G_F}{\sqrt{2}}\ V_{ud}\ \overline{e}\gamma^\mu(1-\gamma^5)\nu_e\ \langle p|\overline{u}\gamma_\mu(1-\gamma^5)d|n\rangle. \tag{2.15}$$

With (2.12), the d-quark could in principle also decay into a charm or top quark, but this is forbidden energetically.

To simplify the problem we assume exact isospin invariance of the strong interaction ($m_p = m_n$) and set the momentum transfer between the baryons equal to zero[3]. Now we can write the matrix element between the nucleon states separated into vector and axial-vector part:

$$\begin{aligned} \langle p|\overline{u}\gamma^\mu d|n\rangle &= g_V\ \overline{p}\gamma^\mu n \\ \langle p|\overline{u}\gamma^\mu\gamma^5 d|n\rangle &= g_A\ \overline{p}\gamma^\mu\gamma^5 n. \end{aligned} \tag{2.16}$$

The full transition matrix[4]

$$T_{if} = -\frac{G_F}{\sqrt{2}}\ V_{ud}\ \overline{e}\gamma^\mu(1-\gamma^5)\nu_e\ \overline{p}\left(\gamma_\mu + \frac{g_A}{g_V}\gamma_\mu\gamma_5\right) n \tag{2.17}$$

contains two unknown parameters, V_{ud} and $\frac{g_A}{g_V}$. Therefore one has to make two measurements to get both values; e.g. the lifetime τ and the asymmetry A from equation 2.27.

2.1.3 Unitarity of the CKM-Matrix

In the standard model of particle physics, the CKM-matrix V is unitary[5]. This means in a simplified picture that the partitioning of the quark fractions is fair, i.e. the sum of the squares of the three parts is always constant.

Apart from the diagonal element, the matrix elements of the third column and the third row are very small. Hence the mixing with the third gereneration is only weak and V_{tb} is almost unity.

Currently, there are three main ways to check the unitarity of the matrix. Although we use only the third one, we mention the others for completeness and since they are important cross checks for the *PERKEO II* results:

Unitarity Triangle: The condition of unitarity $V^\dagger V = 1$ reads in components

$$V_{ij}V_{ik}^* = \delta_{jk}. \tag{2.18}$$

For two specific values, e.g. $j = 1$ (d) and $k = 3$ (b), the equation

$$V_{ud}V_{ub}^* + V_{cd}V_{cb}^* + V_{td}V_{tb}^* = 0 \tag{2.19}$$

builds up a triangle in the complex plane, because each product represents a complex number. This triangle is called unitarity triangle and it can be used to check the unitarity of the elements V_{ij}: If unitarity is not fulfilled the three vectors do not build up a closed triangle.

[3]This can be done, since proton and neutron mass are almost equal, so that the recoil is very small.

[4]If we include the finite momentum transfer between the leptonic and the hadronic current, the hadronic part of the matrix element gets an additional term: the weak magnetism.

[5]Unitary means $V^\dagger V = 1$ with $V^\dagger = {}^T V^*$.

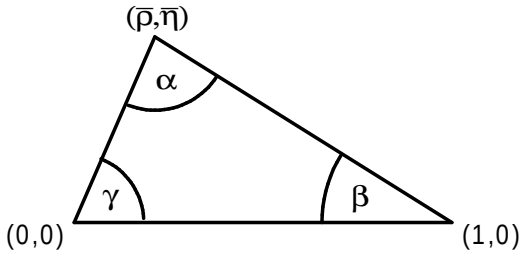

Figure 2.4: Sketch of the unitarity triangle: The three lines build up a closed triangle if the CKM-matrix is unitary. If CP is not violated, all matrix elements are real and the triangle becomes a line.

In the standard form, the base of the triangle is rescaled to unit length (see figure 2.4). Now, the vertices have the coordinates

$$(\overline{\rho},\overline{\eta}) = \left(\frac{\mathrm{Re}(V_{ud}V_{ub}^*)}{|V_{cd}V_{cb}^*|}, \frac{\mathrm{Im}(V_{ud}V_{ub}^*)}{|V_{cd}V_{cb}^*|}\right), \quad (0,0), \quad \text{and} \quad (1,0). \tag{2.20}$$

Combining direct measurements of the matrix elements, results from K- and B-decays, and B mixing processes, the following values for the parameters are obtained [PDG02]:

$$\overline{\rho} = 0.22 \pm 0.10, \quad \overline{\eta} = 0.35 \pm 0.05, \quad \beta = 24° \pm 4° \quad \text{and} \quad \gamma = 59° \pm 13°. \tag{2.21}$$

The values agree with an unitary CKM-matrix within the errors.

Decays of W-Bosons: W-bosons can decay into quark and lepton-pairs; only the top-quark channel is forbidden by energy conservation. The sum of the squares of the six CKM-matrix elements, which do not involve the top-quark, can be determined from the ratio of hadronic to leptonic W-decays [Abe03]:

$$\sum_{\substack{i=(u,c)\\ j=(d,s,b)}} |V_{ij}|^2 = 2.026 \pm 0.026 \pm 0.001. \tag{2.22}$$

This value is consistent with the standard model value $\sum_{ij} |V_{ij}|^2 = 2$ (with $i = (u, c)$ and $j = (d, s, b)$) suggesting the unitarity of the first two rows of the CKM-matrix.

The First Row: Unitarity implies, that the sum of the squares of each column and row has to be unity. This is done for the first row since these values are the most precise:

$$|V_{ud}|^2 + |V_{us}|^2 + |V_{ub}|^2 = 1. \tag{2.23}$$

V_{ub}, measured in semileptonic B-decays, is close to zero so its square can be neglected in the sum. Semileptonic decays of K-mesons give access to V_{us}.

We determine V_{ud} in the neutron decay and combine it with the other two elements from high-energy physics to check equation (2.23).

2.1.4 Angular Correlation Coefficients

To calculate the transition probability $\mathrm{d}\omega$, the matrix element T_{if} (equation 2.17) has to be evaluated and squared. For unpolarized neutrons we obtain

$$|T_{if}|^2 = g_V^2 + 3g_A^2. \tag{2.24}$$

Putting everything into equation (2.3) yields the transition probability

$$\mathrm{d}\omega \propto G_F^2 \, |V_{ud}|^2 \, f^*(E) \, (g_V^2 + 3g_A^2) \, \mathrm{d}E. \tag{2.25}$$

In the case of polarized neutrons, $\mathrm{d}\omega$ can be parametrized into measurable quantities [Jac57]:

$$\begin{aligned} \mathrm{d}\omega \;\propto\; & G_F^2 \, |V_{ud}|^2 \, f^*(E) \, (g_V^2 + 3g_A^2) \, \mathrm{d}E \, \mathrm{d}\Omega_e \, \mathrm{d}\Omega_\nu \\ \cdot \; & \left(1 + a \, \frac{\mathbf{p}_e \mathbf{p}_\nu}{E E_\nu} + b \, \frac{m_e}{E} + \langle \mathbf{s}_n \rangle \left[A \, \frac{\mathbf{p}_e}{E} + B \, \frac{\mathbf{p}_\nu}{E_\nu} + D \, \frac{\mathbf{p}_e \times \mathbf{p}_\nu}{E E_\nu} \right] \right), \end{aligned} \tag{2.26}$$

where $\mathbf{p}_e$ and $\mathbf{p}_\nu$ are the momenta of electron and anti-neutrino, E and E_ν their energies and $\langle \mathbf{s}_n \rangle$ is the neutron spin. The parameters a, A, B and D are called angular correlation coefficients: a is the correlation between the momenta of electron and neutrino, A is the correlation between neutron spin and electron momentum, and B is the correlation between neutron spin and neutrino momentum. The so called "triple coefficient" D is the correlation between $\mathbf{p}_e$, $\mathbf{p}_\nu$ and $\langle \mathbf{s}_n \rangle$. b is the Fierz interference term. Parity is violated as A and B are nonzero. A non-vanishing coefficient D would violate time reversal invariance.

Assuming V-A-theory, all coefficients are functions of $\lambda = \frac{g_A}{g_V}$:

$$a = \frac{1 - |\lambda|^2}{1 + 3|\lambda|^2} \quad A = -2 \, \frac{|\lambda|^2 + \mathrm{Re}(\lambda)}{1 + 3|\lambda|^2} \quad B = 2 \, \frac{|\lambda|^2 - \mathrm{Re}(\lambda)}{1 + 3|\lambda|^2} \quad D = \frac{2 \, \mathrm{Im}(\lambda)}{1 + 3|\lambda|^2}. \tag{2.27}$$

The issue of this thesis is the preparation for a new precise measurement of A.

2.2 PERKEO II

2.2.1 Measuring Principle

The principle of the electron spectrometer *PERKEO II* is fairly simple: A beam of polarized neutrons passes through the spectrometer and some of the particles decay in a certain volume. It is centered within a strong magnetic field ($B_{max} = 1.1$ T), which is produced by two superconducting coils that are close to split pair configuration.

This magnetic field separates the decay volume into two hemispheres and guides the electrons produced in the decay onto two opposing detectors without affecting the neutron beam (see figure 2.5). Hence *PERKEO II* is a real $2 \times 2\pi$ detector where no difficult solid angle corrections have to be applied. Using the count rates of the two detectors, we can determine the experimental electron asymmetry A_{exp}.

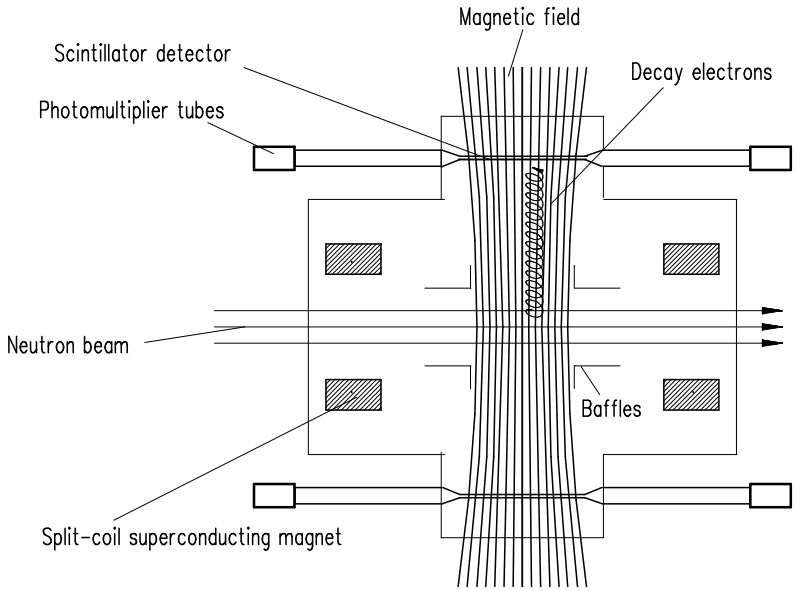

Figure 2.5: The electron spectrometer *PERKEO II*. The gyration radius of the electron is drawn exaggerated.

To polarize the neutrons, we use two supermirror polarizers in a crossed geometry setup to get a polarization degree of almost 100 % [Bre03]. The spin is turned by 180° with a radiofrequency spinflipper during half of the measuring time to reduce systematic errors. We use two scintillators to double statistics and to deal with backscattered electrons, i.e. electrons deposing only a part of their energy in one detector and that are guided by the fieldlines to the other detector afterwards. A coincident readout of both detectors allows the full energy reconstruction of the events.

The experiment will be performed at the cold neutron beam position PF1b at the Institut Laue-Langevin (ILL) in Grenoble, France.

2.2.2 From A_{exp} to V_{ud}

By measuring the electron asymmetry A we average over all anti-neutrino momenta since we do not detect them. Therefore all terms that include $\mathbf{p}_\nu$ in equation (2.26) can be omitted. b is zero in V-A theory so that we get the decay probability

$$\mathrm{d}\omega = f^*(E)\left(1 + A\,\frac{v}{c}\,\cos\theta\right)\,\mathrm{d}E\,\mathrm{d}\Omega_e, \tag{2.28}$$

where θ is the electron emission angle. Due to the division into two hemispheres, integration over $\mathrm{d}\Omega_e$ yields $\langle\cos\theta\rangle = \frac{1}{2}$.

The experimental asymmetry A_{exp} is defined as

$$A_{exp} = \frac{N^\uparrow - N^\downarrow}{N^\uparrow + N^\downarrow} = \frac{1}{2}\frac{v}{c}\,A. \tag{2.29}$$

N is the count rate of one detector where the arrow indicates the direction of the neutron spin. Since neither the polarization setup nor the spinflipper work perfectly, we additionally have to account for the polarization degree $P = \langle s_z\rangle$ of the neutron and the spinflip efficiency $\mathcal{F}$:

$$A_{exp} = \frac{1}{2}\frac{v}{c}\,A\,P\,\mathcal{F}. \tag{2.30}$$

With this result we can obtain the asymmetry A by measuring A_{exp}; but the value still has to be corrected due to several 1%-effects, such as proton recoil, weak magnetism, $g_A - g_V$-interferences and the magnetic mirror effect. Using the second equation in (2.27), λ can be calculated.

Integrating the transition probability $\mathrm{d}\omega$ of unpolarized neutrons (2.25) over the electron energy E yields

$$\omega = \frac{1}{\tau} = C\,|V_{ud}|^2\,(1 + 3\lambda^2)\,f^R\,(1 + \Delta_R), \tag{2.31}$$

where C is a constant, f^R the integral over $f^*(E)$ defined in equation (2.6), and Δ_R are inner radiative corrections. Hence we can determine the value of V_{ud} using the measurements of the lifetime τ and λ.

Results of previous Experiment with *PERKEO II*: The results of the last measurements of the electron asymmetry A in 1997 are published in [Bae96], [Abe97], [Rei99], [Abe02] and [Abe03b]. Since we will repeat this measurements with higher precision, we quote the results to get an impression of the size of the values and the errors:

$$\begin{aligned} A &= -0.1189 \pm 0.0007 \\ \lambda &= -1.2739 \pm 0.0019. \end{aligned} \tag{2.32}$$

Using λ and the world average for the lifetime $\tau = (885.7 \pm 0.7)$ s yields

$$|V_{ud}| = 0.9717 \pm 0.0013. \tag{2.33}$$

Chapter 3

Neutron Beam Collimation

3.1 Collimation and Shielding of Neutrons

The neutron beam has to be directed through the whole experimental setup, which is shown in figure 3.1: Behind the two polarizers, the beam enters the evacuated beamline through a 100 μm aluminium window and passes a radiofrequency spinflipper (chapter 6.1). It enters the spectrometer after a distance of approximately four meters.

Unfortunately, the beam has a certain divergence since the neutron guides (and the polarizers) work via total reflection. The maximal divergence Θ in degrees depends on the reflecting material and is approximately given by

$$\Theta \approx \lambda \cdot m \text{ nm}^{-1}, \tag{3.1}$$

where λ is the neutron wavelength and m a material parameter: The standard nickel neutron guide has $m = 1$, the ILL guides have $m = 2$ and the *PERKEO II* supermirror polarizers $m = 3$. A divergent beam gets bigger as it propagates through the experiment, hence we have to shape it with diaphragms to avoid collisions with the beam tube.

Compared to the last measurement of A in 1997 [Rei99], we can improve the experiment by reducing the radiation background. Radiation is a severe problem since the scintillators cannot distinguish between electrons and photons. Neutrons absorbed in the diaphragms and the beamstop create beam related background. This be subtracted by a measurement without neutrons, hence it should be reduced to a minimum. The collimation system must be installed in a way that the direct neutron beam cannot hit any matter besides the material used for shielding.

Neutron Shielding: Areas frequently hit by neutrons are shielded with ^{6}LiF tiles, since ^{6}Li has a high absorption cross section for neutrons ($\sigma_{n,\alpha} = 940$ b [Nuc95]) in the reaction

$$^6\text{Li} + n \rightarrow ^4\text{He} + ^3\text{H}. \tag{3.2}$$

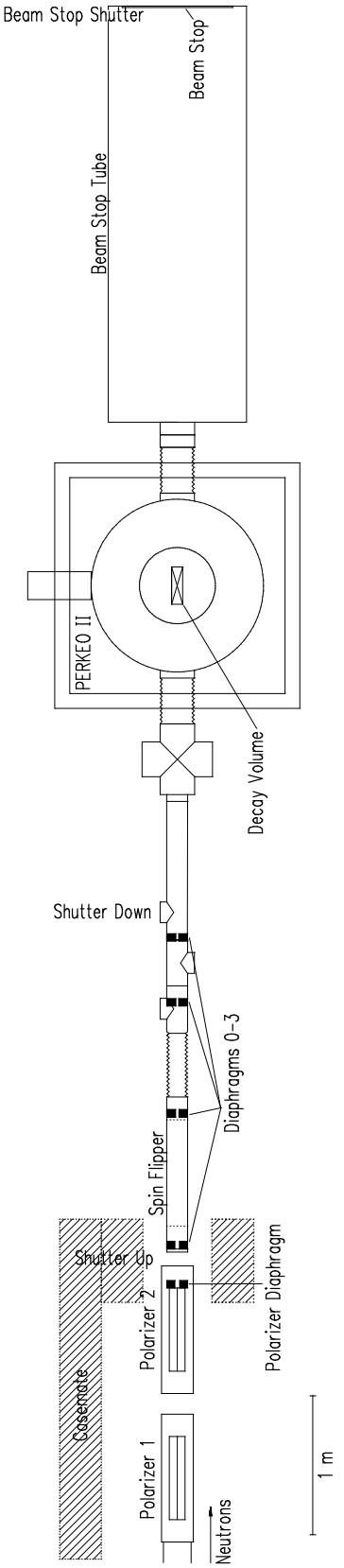

Figure 3.1: *PERKEO II*: The overall experimental setup.

In some of the reactions photons are created, but this effect is suppressed by 10^{-4}. We also use thinner and more elastic lithium rubber to absorb neutrons at less irradiated and curved surfaces. Boron (^{10}B) has an even higher absorption cross section ($\sigma_{n,\alpha} = 3840$ b) but emits a photon in every reaction what should be avoided due to the background problem. Hence we apply normal window glass (borosilicate glass containing ^{10}B) just at areas where only scattered neutrons may occur.

Diaphragms: We use four diaphragms made out of ^{6}LiF tiles to collimate the neutron beam (see figure 3.1). They are glued on 48 mm thick lead bases to absorb the generated γ-radiation. The areas inside the openings, the back plane of the diaphragms, and the outer areas of the front plane are coated with lithium rubber to absorb scattered neutrons. Now, even scattered neutrons cannot hit the lead and produce background what is a big improvement compared to the measurement of 1997, where just the center of the lead base front was covered by ^{6}LiF tiles.

3.2 Monte Carlo Simulation

To obtain the shape and the position of the diaphragms, we wrote a Monte Carlo program that simulates the neutron beam. The program and the physical inputs are presented in this section.

3.2.1 Principle of Monte Carlo Simulations

Monte Carlo methods use random numbers to simulate a problem that may be completely unstatistical in reality. Very often Monte Carlo simulations are used to tackle problems that cannot be solved analytically due to their complexity or because the underlying differential equations are not even known. It is just necessary that the system of interest can be described by probability functions: These contain the information to solve the problem statistically; in our case, the neutron wavelength spectrum is such a probability function.

If a problem is modeled using probability functions, the Monte Carlo simulation proceeds by taking random samples out of these functions to simulate the process. One simulation can be seen as one "observation" and the result is the average over all single trials.

It is very important to use good random number generators to obtain reasonable results. On the other hand a Monte Carlo simulation can just be as good as the probability functions of the problem. Depending on their quality, the results will have an uncertainty of typically several percent.

3.2.2 The Program

The simulation program `MCstrahl` is based on code written by S. Baeßler [Bae03] for a previous *PERKEO II* measurement. We extended its features considerably and adjusted it to the current problem.

It distributes neutrons randomly on the output window of the second polarizer with wavelength and emission angle given by some probability functions. Their geometric path[1] through the experiment is tracked and the neutron distribution on the diaphragms and the beam profile is determined. The count rate of electrons produced in the neutron decay is estimated, therefor the flux of the beam has to be specified. Additionally, the program estimates the rate of fast neutrons that are produced by capture processes in the lithium tiles of the diaphragms.

The following beam geometry can be simulated using `MCstrahl`:

- The neutrons start from a quadratic polarizer window, rotated by 45° in order to simulate the crossed geometry polarization setup.
- One can change the shape of the polarizer using a polarizer diaphragm.
- The collimation system consists of four rectangular diaphragms (diaphragm 0 ... 3).
- The decay volume, i.e. the space in which the β-decay is monitored, has almost the shape of a cuboid.
- To avoid collisions between neutrons and the beam tube, one can specify the position and the size of the transition into the (very big) beam stop tube, the bottleneck of the beamline.
- The neutrons are absorbed in a beamstop.

By varying the size and the position af the diaphragms and the other elements, the most suitable configuration for the collimation system and the best signal to background ratio can be obtained.

[1] For this problem, neutrons can be treated as classical pointlike particles. Scattering and other interactions are not considered by the program.

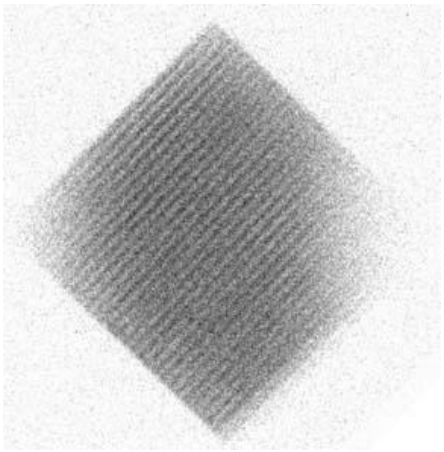

Figure 3.2: Cu-foil activation image of the beam behind the second polarizer seen in reactor direction. The square has the size of the polarizer window: 80 × 80 mm^2. The beam width is 60 mm.

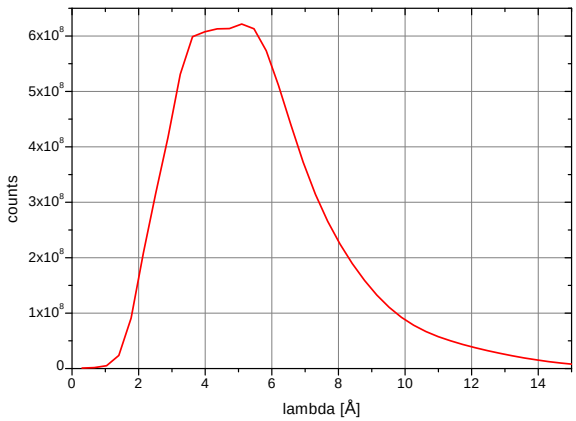

Figure 3.3: Fit function of the $\frac{1}{v}$-weighted wavelength spectrum measured by the *Trine* experiment [Sol03]. This function is used in the simulation program.

3.2.3 Physical Input Parameters

The result of a simulation can only be as good as the physical input parameters that are used to model the problem. In this section, we will describe all the inputs and assumptions included in the program:

Neutron Distribution: The window of the second polarizer is 80 × 80 mm^2 in size and turned by 45°, the neutron guide is 200 mm high and only 60 mm in width. Therefore the simulation starts with an uniform distribution of neutrons on the area covered by both, the polarizer and the neutron guide. Of course, this is not the case in reality: As one can see in figure 3.2, a copper foil activation image of the beam profile after the second polarizer (chapter 6.2.3), the beam is less intense at the boundaries. But since we place a smaller diaphragm (approximately 50 × 35 mm^2) directly behind the polarizer and the beam can be assumed to be constant in this area, this is no problem for the quality of the simulation.

Wavelength Spectrum: The $\frac{1}{v}$-weighted cold neutron wavelength spectrum used for the simulation is shown in figure 3.3. It was obtained during the *Trine* measurement [Sol03] that was performed at the same neutron guide at the ILL. *Trine* only uses one polarizer[2] so this spectrum is just an approximation, assuming that the second polarizer does not change the spectrum significantly.

In chapter 6.2.5 we present the wavelength spectrum after two polarizers. One can see there, that the use of the *Trine* measurement is a good approximation.

[2]This is the polarizer that *PERKEO II* uses as the first one in the crossed geometry setup.

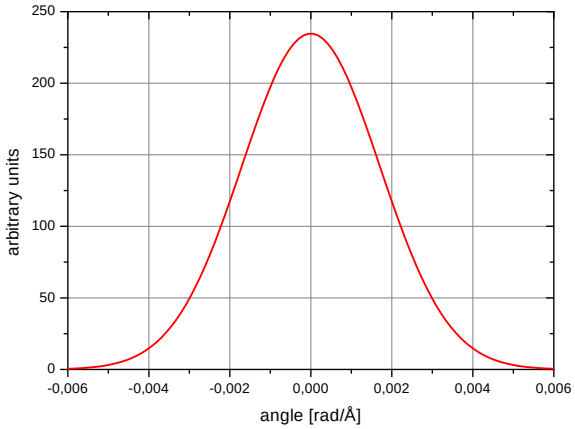

Figure 3.4: The probability function used in the simulation to assign the emission angle per Å to the neutrons. Angles larger than the critical angle Θ are not used.

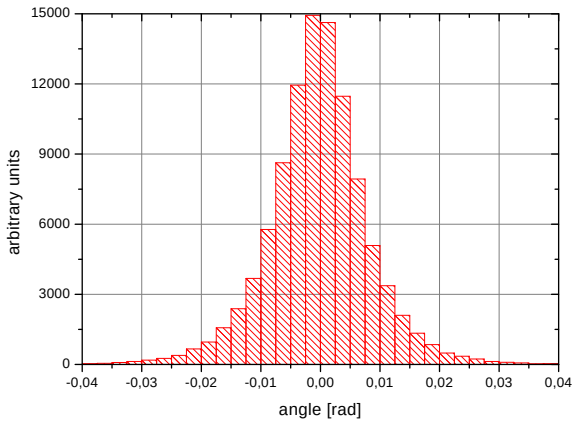

Figure 3.5: Simulation of the angular distribution using the spectrum from figure 3.3. The simulated divergence behind the polarizers is $\sigma = 6.45$ mrad, whereas the measurement of [Mun00] is $\sigma = 6.42$ mrad (without polarizers).

Angular Distribution: Assigning the emission angle to the neutrons as they start from the polarizer is the most crucial point in this simulation, since it has never been measured. We assume a gaussian distribution with a standard deviation

$$\sigma = \frac{\Theta}{2.8}, \tag{3.3}$$

(see figure 3.4), where Θ is the critical angle of the polarizer in rad/Å and the factor 2.8 is adjusted to a measurement of the divergence of the neutron guide without polarizers [Mun00] in a way, that the measured and the simulated divergence of the whole beam coincide (figure 3.5).

The assumption that the polarizers are not influencing the beam divergence is weak and since the measured flux behind the last diaphragm is lower than simulated (chapter 6.2.4), we know that the real angular distribution must be somewhere between this one and a uniform distribution, which yields a count rate reduced by 62 %.

Neutron Flux: We detect neutrons with He-Gas counters or gold foil activation. Both methods have a $\frac{1}{v}$-detection efficiency since the interaction probability is proportional to the neutron velocity v. The neutron wavelength λ is related to the velocity v with the formula

$$\lambda = \frac{3956}{v} \text{ m s}^{-1}\text{Å}, \tag{3.4}$$

i.e. neutrons with long wavelengths λ are detected favouredly.

Hence we do not measure the absolute flux

$$\phi = \int_v \phi(v)\ \mathrm{d}v \tag{3.5}$$

with these detectors but we detect the $\frac{1}{v}$-weighted capture flux

$$\phi_c = \int_v \phi(v)\ \frac{v_0}{v}\ \mathrm{d}v \tag{3.6}$$

where $v_0 = 2200$ m s^{-1} is the thermal velocity. Because of this, the capture flux is also called "thermal equivalence flux". For cold neutrons the absolute flux is lower than the capture flux since $v < v_0$.

In the simulation, we assume a capture flux of $\phi_c = 2 \cdot 10^9$ s^{-1} cm^{-2} behind the second polarizer.

Fast Neutrons: A small fraction of the neutrons hitting the ^{6}LiF-tiles or lithium rubber produces fast neutrons in a ^{6}Li(n,^{3}H)^{4}He reaction. These have to be moderated with polyethylene and shielded with boron rubber. Otherwise they get moderated by the helium that cools the magnet and can create background radiation.

Measurements show that 10^6 thermal neutrons (energy $E \approx 25$ meV) produce (93$\pm$10) fast neutrons on ^{6}LiF [Lon80]. Since the cross section scales with $\frac{1}{v} \propto \frac{1}{\sqrt{E}}$, this information is sufficient to estimate the production rate for cold neutrons what is done by the simulation program for each diaphragm and the beamstop.

3.3 Optimization and Results

Optimizing the collimation system is an interplay between achieving high electron count rates and low background radiation. The latter is created by neutrons hitting the ^{6}LiF-tiles and by scattering on the diaphragms; therefore background reduction can be achieved by using diaphragms far away from the decay volume so that the solid angle of the diaphragm area seen from the detectors is as small as possible. But since the overall beam size is determined by the beam tubes, the opening of the diaphragms has to be decreased when shifted away from the spectrometer, causing a lower count rate.

The background should be as small as possible for this run of *PERKEO II*, hence its reduction has higher priority in the optimization process. The background from the diaphragms is proportional to d^{-2}, where d is the distance of the diaphragm from the detector. Since it is also proportional to the number of neutrons hitting the diaphragm, this number should be minimized on the last one.

Using the program `MCstrahl` and simulating one million neutrons we get the following result for the optimized collimation system. It gives the size[3] and position of the beam

[3] In this thesis, we use the standard coordinate system for neutron guides: The neutrons propagate in z-direction, x is the horizontal and y the vertical coordinate; the system is right-handed.

elements (in millimeters), the percentage of neutrons hitting them and the production rate of fast neutrons:

	distance [mm]	x [mm]	y [mm]	neutrons [%]	fast n [kHz]
polarizer diaphragm	0	48.0	34.0	67.32 ± 0.11	6080
diaphragm 0	282	46.0	32.0	4.70 ± 0.02	428
diaphragm 1	1232	36.0	24.0	14.53 ± 0.04	1303
diaphragm 2	2032	33.4	19.9	5.67 ± 0.02	467
diaphragm 3	2499	34.4	20.4	1.29 ± 0.01	98
decay volume	5064	126.2	80.0	6.49 ± 0.03	-
beamstop	9241	-	-	6.49 ± 0.03	5547
count rate: (720 ± 27) Hz		(Flux: $2 \cdot 10^9$ cm^{-2} s^{-1})			

With these diaphragm sizes we obtain a decay volume of 126.2 × 80.0 × 270 mm^3. Assuming a capture flux of $2 \cdot 10^9$ cm^{-2} s^{-1} on the second polarizer, we expect a count rate of (720 ± 27) Hz. This rate 10 % higher than simulated with the setup of 1997, whereas the background from the last diaphragm is reduced by 92 % since we shifted diaphragm 3 away from the scintillators to obtain a smaller solid angle and optimized the other diaphragms.

Figure 3.6 shows the simulated beam profile on the four diaphragms in this configuration. Figure 3.7 shows horizontal and vertical cuts through the center of the diaphragms. The simulation is expected to be accurate within 10 to 20 %.

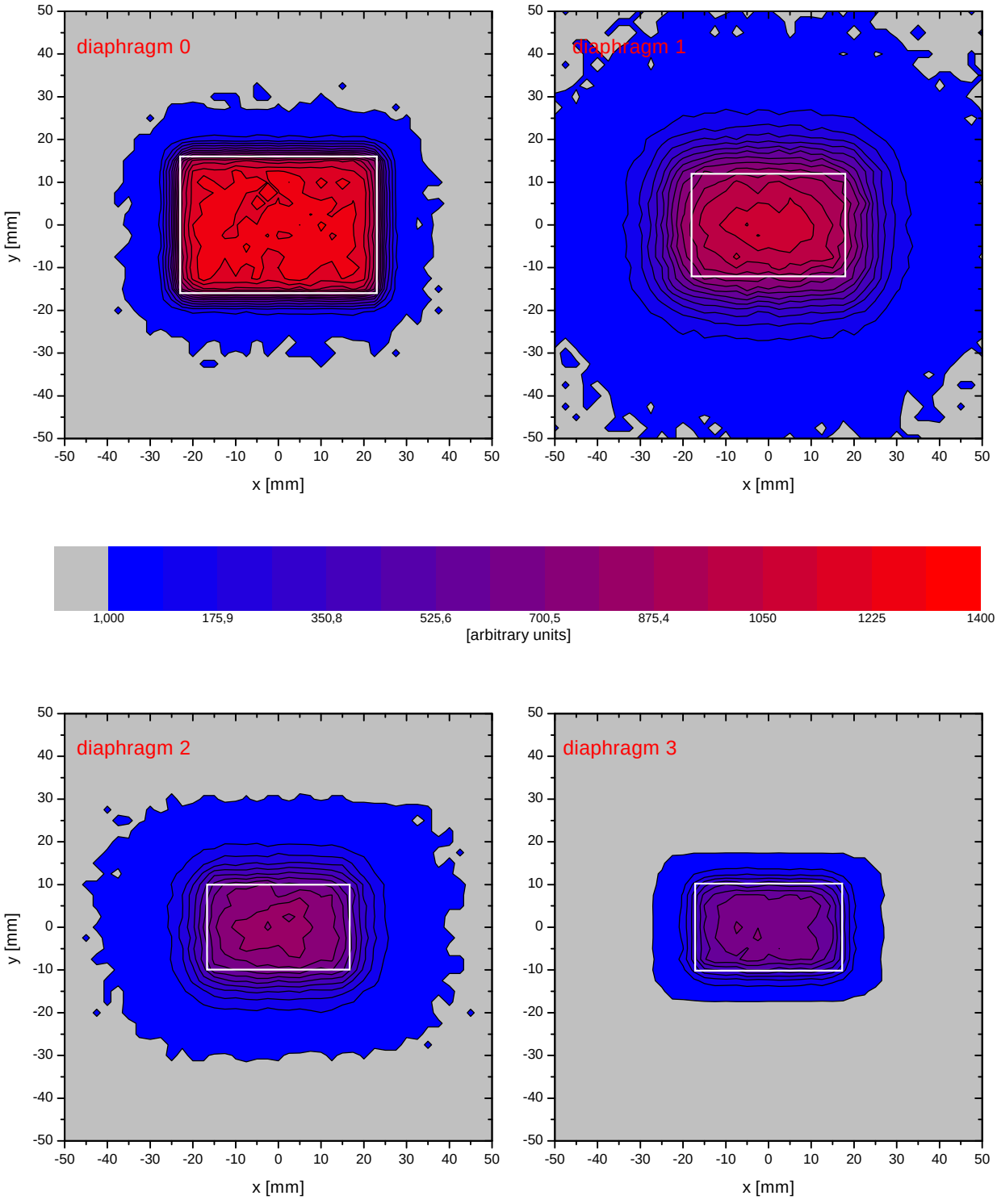

Figure 3.6: The beam profile on the diaphragms obtained by a Monte Carlo simulation tracking 10^6 neutrons. The white rectangles indicate the size of the diaphragm openings. The grey region is not hit by neutrons.

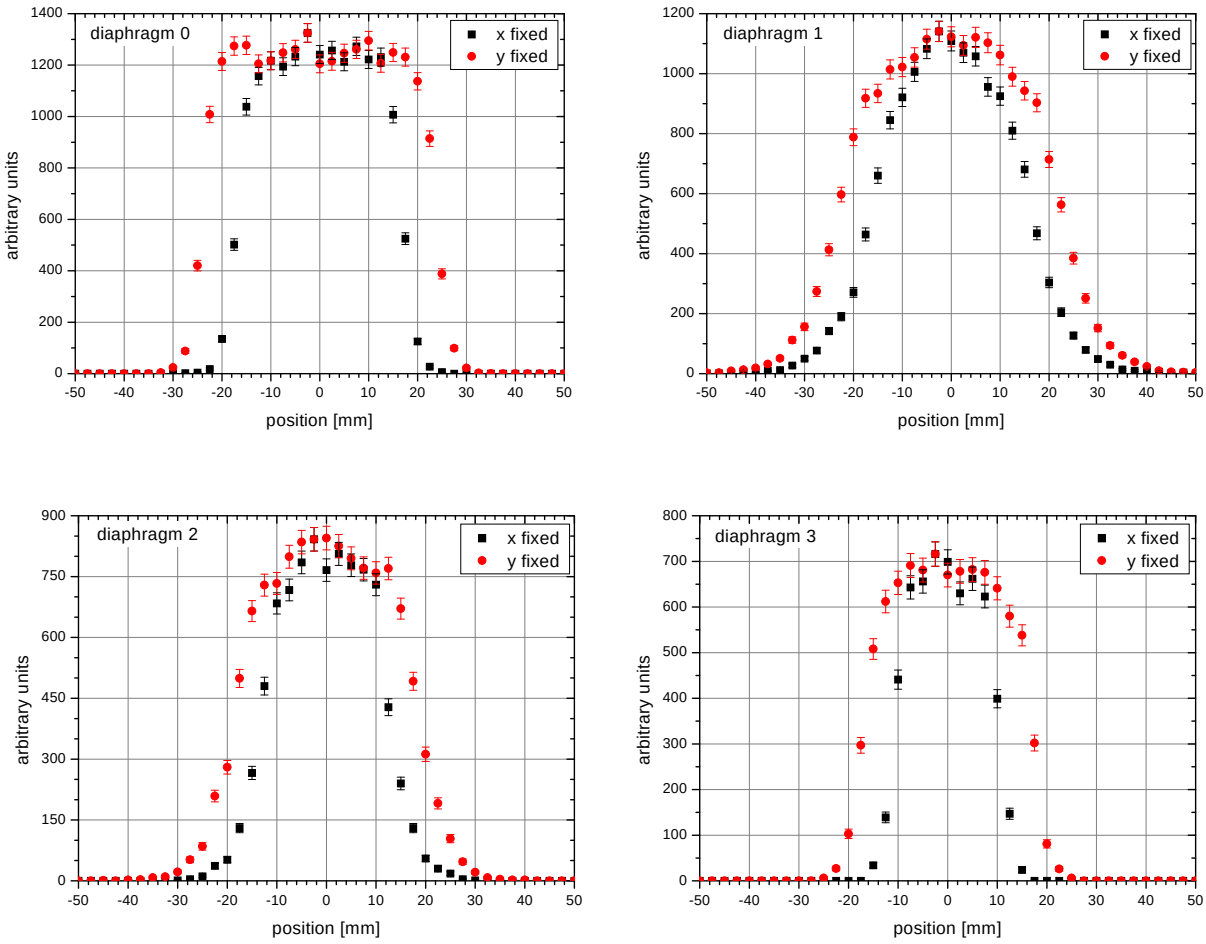

Figure 3.7: Horizontal and vertical cuts through the center of the simulated beam profile on the four diaphragms.

Chapter 4

Detector Tests

PERKEO II uses two 440 × 160 mm^2 BICRON 404 plastic scintillation detectors that convert the electron kinetic energy into light. For each scintillator, the photons are directed to four mesh photomultipliers HAM R5504 from HAMAMATSU via plexiglass guides. The photomultiplier tubes are inside the vacuum system and have to work in the magnetic field of the spectrometer, which is approximately 200 mT at their position.

Understanding the detector system and its response on an event is essential for a precision experiment. Therefore we performed test experiments without neutrons to determine its performance. We present a new device to examine the detector function and the results of the measurements in this chapter.

4.1 The YZ-Scanner

During the last experiments with *PERKEO II*, the energy calibration of the detector system was done with two calibrating caroussels: Each of them consists of a half disk containing three radioactive sources in separated positions, so it is possible to expose the detectors to only one or no calibration source, depending on the angles of the caroussel disks. Unfortunately is it not possible to detect spatial effects in the detector function with this system. During the last A measurement, the spatial resolution was determined in a non-evacuated setup after the data acquisition. Hence we were not able to monitor spatial changes in the detector function during the measurement.

Therefore a two dimensional calibration system, which works additionally to the caroussels inside the vacuum vessel, was developped [Bre03]: the YZ-Scanner, shown in figure 4.1. With this setup it is possible to obtain the dependence of the detected electron energy on the point where the electron has hit the scintillator. Scintillation light emitted in the center of the detector has to suffer higher losses due to the longer path to the photomultipliers compared to light produced close to the plexiglass guides. Therefore an electron from the

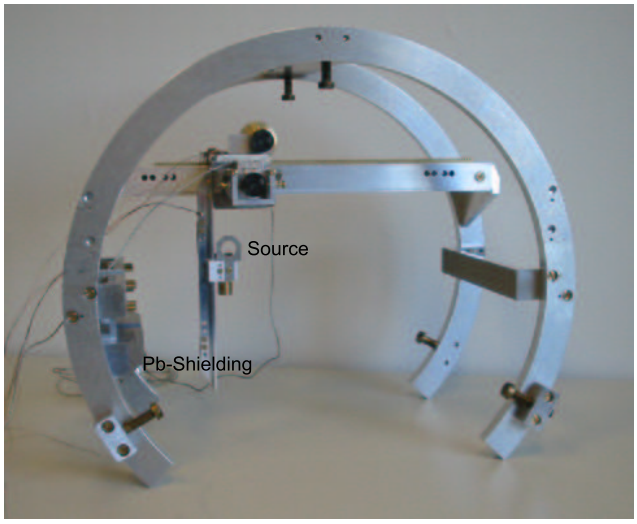

Figure 4.1: The YZ-Scanner, a two dimensional calibration system to obtain the dependence of the detected electron energy on the interaction point with the scintillator. It is placed next to the decay volume and the neutrons propagate parallel to the horizontal carriage.

detector center seems to have lower energy than the same electron hitting the scintillator at the outer areas.

The scanner consists of a carriage moving in z-direction and a smaller one attached to the first for the y-motion. Both are driven by piezo motors that work in high magnetic fields. The device is operated via a controller connected to the USB port of the measurement computer.

Compared to the status of the YZ-Scanner described in [Bre03], we had to make some optimizations to ensure its usability within the vacuum system and in the magnetic field of almost one Tesla:

- The framework of the device was shortened in x-direction (perpendicular to the detectors) to ensure that the decay electrons cannot collide with the scanner due to the expanding field lines (see also chapter 4.2).
- Tests indicated that a simple potential divider to obtain the z-position of the carriage does not work inside the vacuum vessel, probably because of the reduced friction. Hence we replaced it by a toothed wheel, which is connected to a potentiometer and moves on a toothed rack.
- The lead shielding of the calibration source was moved to a point below the xz-symmetry plane where no interference with the decay electrons is possible. It was also enlarged to reduce the background from the source on the scintillators.

4.2 Expansion of the Decay Volume

The magnetic field lines inside the decay volume, which is centered in the spectrometer, are homogeneous but they expand in the direction towards the detectors. Hence the image of the decay volume on the scintillators is enlarged since the decay electrons follow the magnetic field lines. So the decay volume has to be small enough to ensure that all electrons reach the detectors; on the other hand it should be as large as possible to get a high event rate. We examine this problem in a theoretical way based on numerical calculations of the magnetic field [Mun03]. The corresponding measurements are presented in chapter 4.3.3.

Electrons in an inhomogeneous Magnetic Field: As the electrons move along the field, they perform a gyrating motion around the field lines with the frequency

$$\omega_B = \frac{eB}{\gamma mc}, \tag{4.1}$$

where e is the electron charge and m its mass, B the magnetic field, $\gamma = \sqrt{1-(v/c)^2}$ the usual relativistic factor and c the speed of light. If electrons with energy E (in units of the rest mass) are emitted perpendicular to the field we can estimate the gyration radius r_B using

$$r_B = \frac{1.70\sqrt{E(E+2)}}{B} \text{ mm T.} \tag{4.2}$$

While the gyration effect is well known from homogeneous fields, a spatially variable field additionally induces a drift motion to the electron [Jac02]: The electron spirals around a field line when the latter changes its direction. This is equivalent to a centrifugal acceleration and causes a so called curvature drift of the velocity

$$\mathbf{v}_C = \frac{v_{||}^2}{\omega_B R}\frac{\mathbf{R}\times\mathbf{B}}{RB}, \tag{4.3}$$

with the curvature radius $\mathbf{R}$ of the field and the velocity parallel to the field lines $v_{||}$.

Estimation for *PERKEO II*: Formula (4.2) shows that the gyration radius r_B increases with higher electron energy E and the reduction of the field B. Using the smallest value $B \approx 0.55$ T obtained at the scintillators[1] and the maximal electron energy in neutron β-decay $E_{max} = 782$ keV yields a maximal gyration radius $r_B = 7.2$ mm.

We get the maximum curvature drift (4.3) for small curvation radii R. Estimating $R \approx 1300$ mm from the simulated field and assuming that $v_{||}$ contains all kinetic energy, we obtain

[1] All absolute magnetic field numbers in this chapter are estimated using numerical calculations performed by [Mun03].

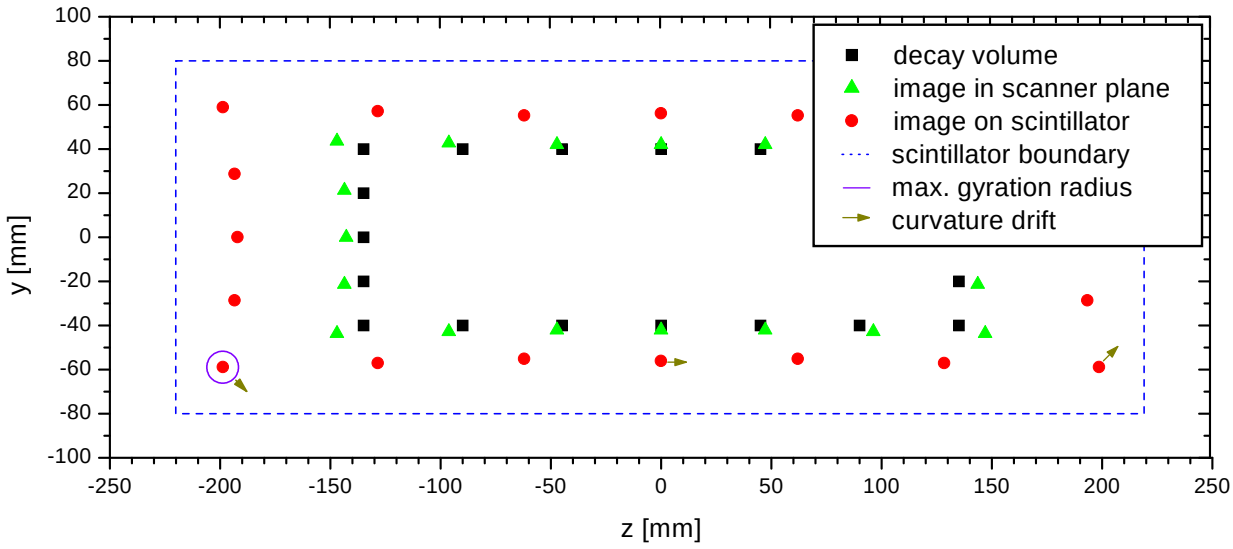

Figure 4.2: Images of the expanding decay volume in YZ-Scanner distance (237 mm from beam center) and on the scintillators (480 mm); the spatial error is ± 2 mm in both directions since the values are estimated from numerical calculations. The circle indicates the maximal gyration radius and the arrow gives the direction of the curvature drift at some points. The deflection is approximately 1 mm and can be neglected.

$v_C = 5 \cdot 10^5$ m s^{-1} causing a displacement of approximately 1 mm at the scintillator. Since the estimation is rather conservative, the curvature drift can be almost neglected.[2]

The expansion of the decay volume due to the inhomogenious magnetic field is shown in figure 4.2. Since the magnetic field strength is just interpolated from numerical simulations, we assume an error of ±2 mm in the position on the scintillator for each point. The figure demonstrates that there is no problem with a decay volume of 270 mm lenght and 80 mm height (the x-dimension is just limited by the magnetic mirror effect and the beamline); the image in the YZ-Scanner plane was important to determine the position of the Pb-shielding of the scanner calibration source.

4.3 Test Measurements of the Detector System

These measurements were performed in the new experiment hall of the physics department in Heidelberg. We attached just one scintillation detector with four photomultipliers to the spectrometer and placed the YZ-Scanner equipped with a weak bismuth (^{207}Bi) β-source[3] exactly in the middle of the decay volume. The whole setup was evacuated on the

[2] An additional effect in inhomogenious fields is the gradient drift. It is proportional to $\frac{1}{2}v_\perp^2$ and causes a deviation in the same direction as the curvature drift. Since we assume that $v_\parallel$ contains all kinetic energy for the conservative estimation, we can neglect the smaller gradient drift.

[3] The conversion electron source ^{207}Bi has a line spectrum.

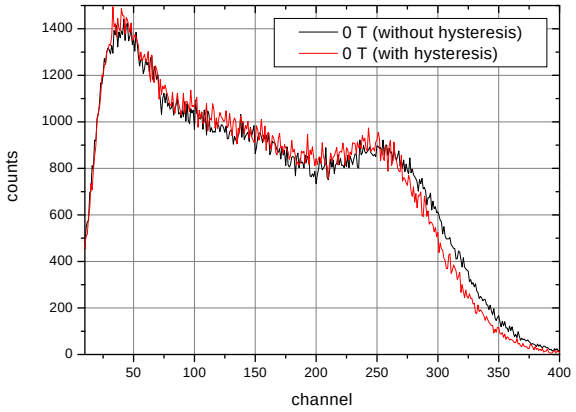

Figure 4.3: Photomultiplier spectra of ^{60}Co with and without hysteresis effect. The spectra have a very low resolution due to the unknown behaviour of the used NaI-scintillator.

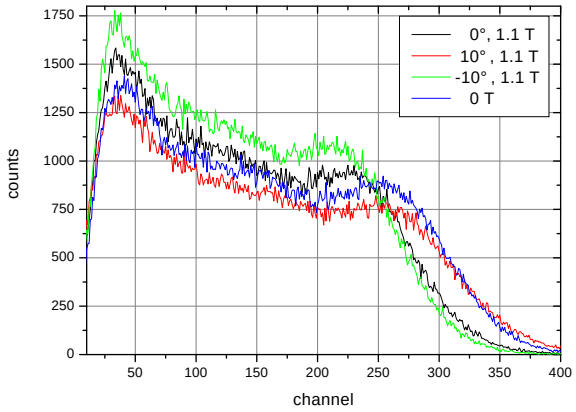

Figure 4.4: ^{60}Co γ-spectra measured at different angles[4]. The amplification is not changed for an angle between 0° and 10°.

10^{-6} mbar level and the magnetic field was varied according to the focus of interest.

Due to an insufficient photomultiplier fixation system some measurements were performed with only three of the tubes because one of them was not coupled properly to the plexiglass light guide. To avoid light losses, we applied vacuum grease between the plexiglass and the photomultipliers.

4.3.1 Orientation of the Photomultipliers

The mesh photomultipliers work in a magnetic field [Plo00] but the amplification depends on their orientation in the field. To determine the gain of the whole detector we need the same amplification with the magnet switched on and off. Since the position of the photomultiplier tube is fixed by the scintillator and the light guides we had to change its angle[4] inside the field to optimize its gain.

It is important to consider the hysteresis of *PERKEO*'s steel shielding: Figure 4.3 demonstrates that the photomultiplier spectrum depends on the history of the magnetic field. Hence we always measure with the field switched on first and turn it off afterwards.

The γ-spectra of the weak ^{60}Co source (figure 4.4) were obtained using just one photomultiplier directly attached to a NaI-scintillator; the setup was placed at the real position but not in vacuum. Due to an unknown reason the resolution is very poor and the spectra do not look like ^{60}Co at all. Nevertheless, we were able to use the spectra because we are

[4]The cathode of the photomultiplier tube is connected to the light guide. We change its angle in the magnetic field by moving its rear in the xz-plane. An angle of 0° indicates that the photomultiplier is aligned with the neutron beam. The angle is positive if the tube end is moved towards the beam.

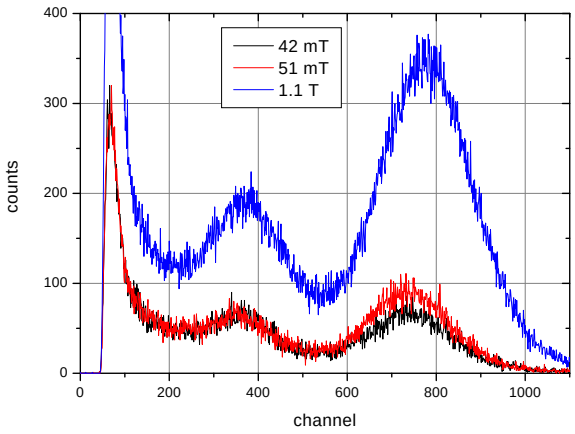

Figure 4.5: Spectra of ^{207}Bi measured at an angle of 5° with different magnetic fields. One can see a slight shift of the peak position. The count rate decrease is due to the much larger gyration radius at low fields.

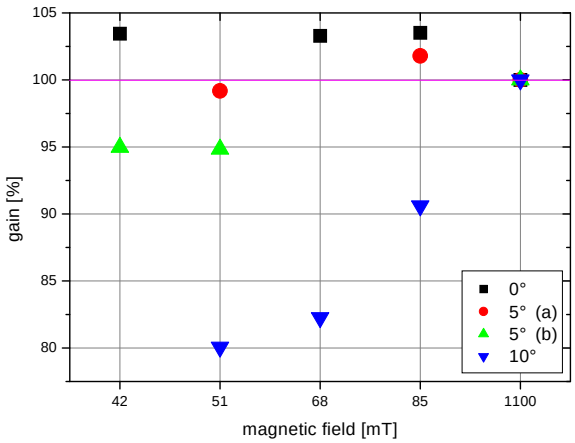

Figure 4.6: The detector gain for different angles normalized to the full field of 1.1 T. It is constant for an angle between 0° and 5°.

only interested in the amplification change and because we got the same wide peak for all measurements. We determined the peak position by Gauss fits. The result is that the amplification is constant for an angle between 0° and 10°.

Additionally, we measured spectra of ^{207}Bi at different angles (0°, 10° and two times 5° with different statistics; a positive angle indicates, that the end of the photomultiplier is turned towards the neutron beam) for high and low magnetic fields using the *PERKEO II* plastic scintillator and three to four photomultiplier tubes in vacuum. Since there is no peak visible for 0 T, we had to measure at very low magnetic fields and to extrapolate to zero. Figure 4.5 shows the spectra at 5° with high statistics - one can see the shift of the upper peak.

For all measurements, we fitted the upper Bi-Peak using a Gauss function as approximation. The detector gain normalized to the maximum magnetic field (1.1 T) is illustrated in figure 4.6: For 0° the gain at low fields is slightly higher than at 1.1 T, for the second 5° measurement (b) with high statistics and four photomultipliers it is a little bit too low. Hence we will fix the photomultiplier tubes at an angle of 3° during the experiment.

4.3.2 Detector Drift

It is important for the systematics of the measurement that the photomultiplier amplification is constant in time. We made a 12:40 hours measurement to check this behaviour and plotted the position of the upper ^{207}Bi peak in figure 4.7. It shows a linear shift of 3.5 channels to higher energies.

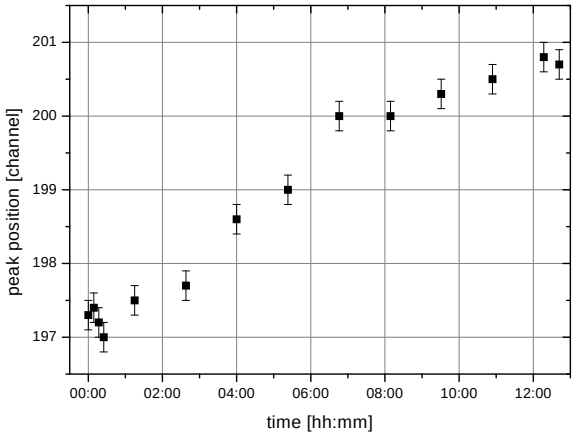

Figure 4.7: Drift of the upper ^{207}Bi peak during 12 hours.

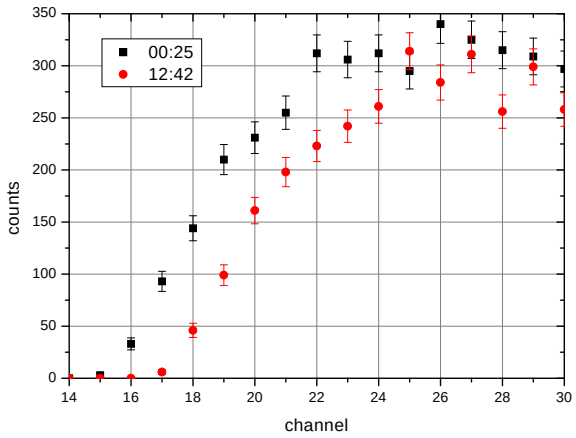

Figure 4.8: The main part of the drift is not due to a change in the detector gain but due to an offset in the electronics.

The drift is not solely caused by a change of the amplification because this would not modify the spectrum at low energies. In this region the whole spectrum is shifted (figure 4.8) and we obtain an offset of 2 channels. Since we perfomed the measurement without temperature-stabilized electronics, this effect should be absent with electronics in an air-conditioned environment. Moreover, we will have very short data acquisition cycles (minutes) with calibration measurements in between, thus a detector drift time of several hours constitutes no problem.

4.3.3 Spatial Dependence of the Efficiency

When an electron hits the scintillator, a part or all of its energy is converted into photons. These propagate inside the scintillator and the light guides via total reflection, finally reaching the photomultiplier tubes where they extract electrons out of the cathode due to the photoelectric effect. The loss of photons is proportional to the number of total reflections hence the amount of light detected by the photomultipliers depends on the position where the incident electron has hit the scintillator. This behaviour was examined with the YZ-Scanner:

y-Direction: Figure 4.9 shows the position of the upper ^{207}Bi peak at different y-positions. We did the measurements with the full magnetic field of 1.1 T at a photomultiplier angle of 0°. Since only three of the four photomultipliers were working, we could solely use the side with two intact tubes for the analysis to see the y-dependence: We obtain a plateau of almost 80 mm width, then a decrease in efficiency.

In chapter 4.2 we derived the image of the decay volume from numerical simulations. Figure 4.10 confirms that a decay volume of 80 mm height can be projected onto the scintillator without problems.

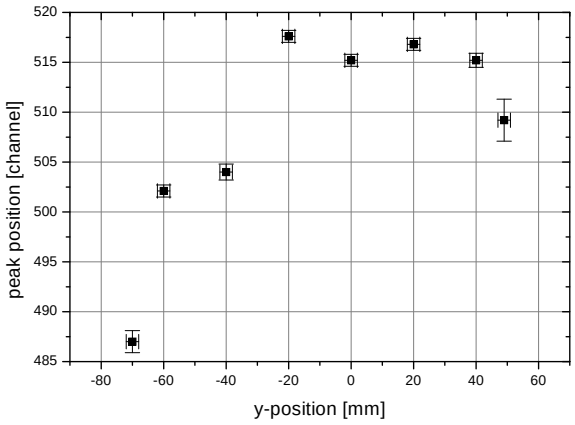

Figure 4.9: Dependence of the efficiency on the y-position of the source. The measurement was performed using just two photomultipliers on the same side of the scintillator and shows a plateau of almost 80 mm width.

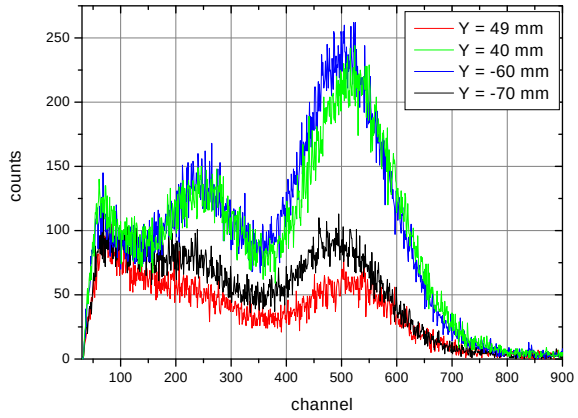

Figure 4.10: Spectra of the two photomultipliers: The electrons from the positions y = 49 mm and y = −70 mm do not reach the scintillator properly, so the maximal height of the decay volume should be smaller than 100 mm.

z-Direction: The measurements of the z-dependence were performed at 5° and with a field of 170 mT due to a lack of helium to cool the magnet. We were only able to obtain values at five positions (figure 4.11) because a vacuum pump crashed during the experiment. Nevertheless a fit of a quadratic function is possible (reduced $\chi^2 = 0.9983$). Comparing the scintillator border with the minimum of the fit curve yields an efficiency decrease of 16.2 % which constitutes no problem for the detector system.

We make a quadratic fit to the data with the point at 53 mm shifted 2 σ down to check the result because of the small amount of data. Here we obtain a decrease of 15.0 % which is consistent with the value above.

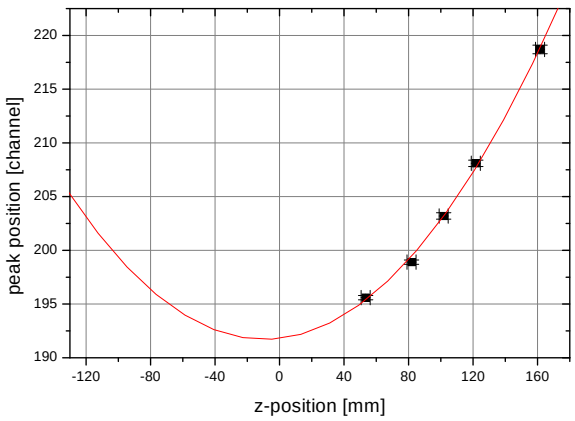

Figure 4.11: Dependence of the efficiency on the z-position of the source. Unfortunately not more data could be obtained. Nevertheless a quadratic fit is possible so that we expect a maximal efficiency loss of 16.2 %. The minimum of the curve is not at the center position of the decay volume (0 mm), because the scintillator was not centered in z-direction.

4.3.4 Detector Resolution

One important parameter for the detector resolution is the number of photoelectrons (PE) produced in the photomultiplier cathode per MeV electron energy deposed in the scintillator. The more photoelectrons the better is the detector resolution since it is easier to distinguish between closely lying lines.

We used little plexiglass connectors between light guides and photomultipliers to obtain the different angles in the magnetic field. Unfortunately, these bring along another discontinuity in the light guide causing photon scattering and additional light losses because they had two non reflecting surfaces. Nevertheless, we can do a simple loss estimation using a rod-model for the scintillator and the light guides:

	optimistic	pessimistic
scintillator (BIC 404) generates 14 000 PE/MeV		
transmission scintillator ($e^{-\lambda x}$)	0.80	0.70
transmission light guide	0.90	0.80
solid angle (rod model)	0.17	0.17
glue (scintillator - light guide)	0.92	0.86
glue (light guide - 5° connector)	0.92	0.86
glue (5° connector - photomultiplier)	0.92	0.86
quantum efficiency photomultiplier	0.25	0.22
N	334 PE/MeV	187 PE/MeV

The number of photoelectrons per MeV can be measured using the 4-difference method [Mue96] that allows to subtract the photons from the β-source and the environmental background to determine the pure electron spectrum. We measure the following spectra:

S_B	source (S) with magnetic field ($B = 1.1$ T)
0_B	shielded source (0) with magnetic field (B) to obtain the environmental background
S_0	source (S) without field (0) to suppress electrons and photons
0_0	shielded source (0) without field (0).

Then the 4-difference spectrum S_4 is defined to be

$$S_4 = S_B - 0_B - S_0 + 0_0. \tag{4.4}$$

Figure 4.12 shows the four ^{207}Bi spectra for a photomultiplier angle of 5°.

The following is an order of magnitude estimation and we assume the upper bismuth peak to be at 1 MeV. Since ^{207}Bi is an electron capture source there are a lot more lines in reality: for K-shell capture at 975.7 keV, for L-shell capture at 1048.3 keV and at 1061.2 keV if

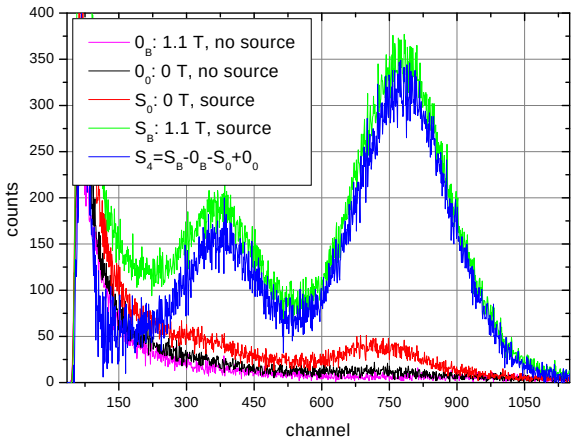

Figure 4.12: Spectra for a 4-difference analysis obtained at an angle of 5°. This analysis allows to extract the pure electron spectrum from the measurement, suppressing photons from the source and the environmental background. The resolution of the detector can be derived from the width and the position of the upper ^{207}Bi-peak in the S_4 spectrum.

the electron comes from the M-shell [Arn87]. Due to the subsequent emission of Auger electrons these lines also consist of several sub-lines. An average value for the measurable line is 996.9 keV.

From a Gauss fit to the S_4 spectrum we obtain the peak position at channel $x_0 = 778.6 \pm 0.6$ with a pedestal[5] $p = 41.0$. The width of the peak is $\sigma = 97.8 \pm 2.3$ hence we get the resolution which is given by Poisson statistics:

$$\frac{\sigma}{x_0 - p} = 0.133 \pm 0.003 \stackrel{!}{=} \frac{1}{\sqrt{N}}. \tag{4.5}$$

Solving for N, the number of photoelectrons per MeV, we obtain $(N = 57 \pm 3)$ PE/MeV.

A 4-difference measurement at 0° without plexiglass connectors, which corresponds to the setup for the A measurement where the light guide itself is beveled to 3° making the connectors unnecessary, yielded $(N = 90 \pm 5)$ PE/MeV for three running photomultipliers. Hence we expect $(N = 120 \pm 6)$ PE/MeV when we measure with four photomultipliers per detector. This is a satisfactory number for a detector setup with photomultiplier readout at the scintillator sides.

The number of photoelectrons in the 5°-measurement is so low due to well known effects [Plo00]: Each contact surface of different materials glued together using vacuum grease brings along a light attenuation of more than 10 %. This number increases if there are air bubbles inside the grease. In our measurement, the light losses are additionally enlarged due to dirt on the scintillator and the light guides reducing total reflection and due to insufficient fixation of the scintillator ("glue lakes") and the photomultiplier tubes. Moreover, the plexiglass connector pieces had two non-reflecting surfaces that suppress total reflection.

[5]The pedestal is the sum of the photomultiplier channels when no signal is applied.

Chapter 5

Data Acquisition System

Data acquisition means the conversion of the analog photomultiplier signals to digital values and their transfer to the computer, together with other digital data from the electronics system, e.g. timing informations. In this chapter, we describe the electronics setup and the software to read and analyze the data and to control the experiment.

5.1 Electronics Overview

The electronics setup of the *PERKEO II* experiment is sketched in figure 5.1: We use two scintillation detectors, each attached to four photomultipliers. On the one hand the analog signals generated by an event get delayed and transferred to the analog to digital converters (ADCs), on the other hand they are converted to digital pulses with discriminators and enter the digital branch of the setup if at least two signals are detected by one of the coincidence units simultaneously. This branch is used to enable the electronics modules described below and to obtain informations about the event.

We use the following electronic devices, which are indicated as ellipses in the figure, to process the incoming events. All these modules have to be controlled and read out by the data acquisition program:

- **Analog to Digital Converter (ADC):** Since we have 8 photomultipliers we also use 8 charge integrating ADCs to convert the analog signals to digital numbers.
- **Time to Digital Converter (TDC):** A TDC converts the time interval between a gate edge and a trigger signal or between two triggers into a digital value. We use two TDC channels (one for each detector) with a shared gate to decide which detector has seen the first signal. Hence we can determine backscattering effects, where an electron deposits its energy only partially in one detector and is backscattered to the other.

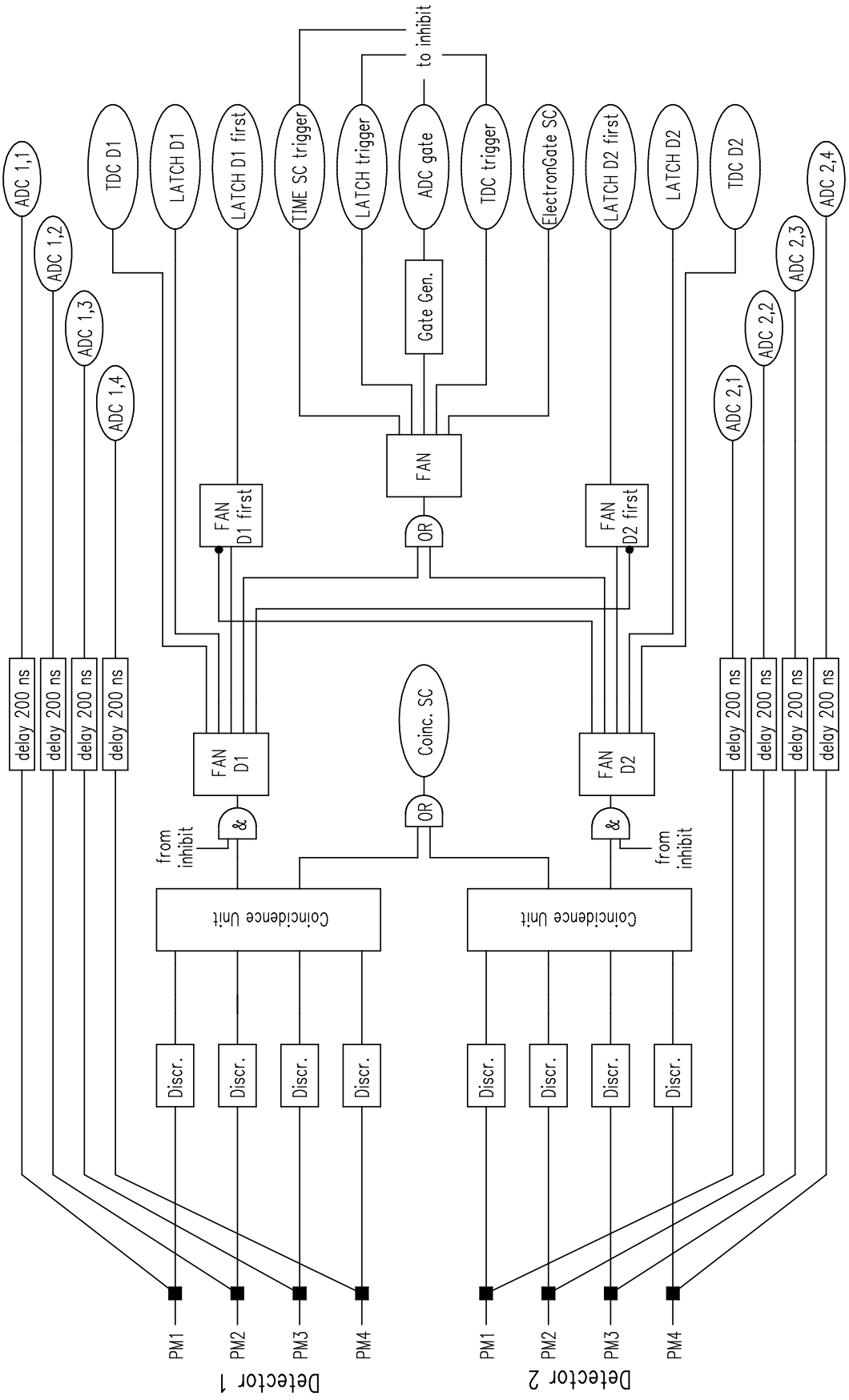

Figure 5.1: Sketch of the electronics setup of the *PERKEO II* experiment.

- **Latch:** A latch is a device that reads a bit pattern from its inputs when triggered. We use one latch with 4 input channels to record which detectors registered a signal and in which order.

- **Time Counter (TIME SC):** Our time counter is a simple TDC: It has an internal clock that is started with a gate and whose value is written into a register when a trigger signal is applied. We use the time counter to obtain a global time for each event to be able to detect systematic effects like afterpulses from the detector system.

- **Scaler (SC):** A scaler is a counter that increases its value by one whenever it is triggered. It is used to count the measuring time, electron gates, neutrons etc. Altogether, we apply 12 scalers.

- **Digital IO:** A digital input/output register allows to set individual outputs high or low. We use it to enable the whole electronics system and to operate the spinflipper.

5.1.1 ADC-Linearity

With the spectrometer *PERKEO II*, we measure energy dependent spectra of the decay electrons, hence we need ADCs with a good linearity. Since we apply the VME-ADCs, which were build by the electronics laboratory of the Physics Institute Heidelberg, for the first time we made measurements on their linearity. To control the charge on the ADCs very precisely, we used rectangular pulses of fixed height and several nanoseconds length as input signal.

The non-linearity L is defined to be

$$L = \left| \frac{\Delta C}{C_{max}} \right| \tag{5.1}$$

[Leo94], where C_{max} is the maximal measured channel and ΔC the maximum deviation from the linear fit. Our ADCs should have a non-linearity below 1 %. The measurements for 9 ADCs (there are 3 ADCs on each module) are presented in figure 5.2. We always give two values for the non-linearity L: The first one includes the measurement without gate, the second ignores this value since it will show a deviation if every gate has a constant offset in length. Therefore the second non-linearity value is always a little bit smaller.

This number for the non-linearity L, which is always equal or below 0.40 %, is more realistic, because each ADC reads at least a constant offset (the pedestal) during the experiment. Hence we should have no problems with the ADC linearity.

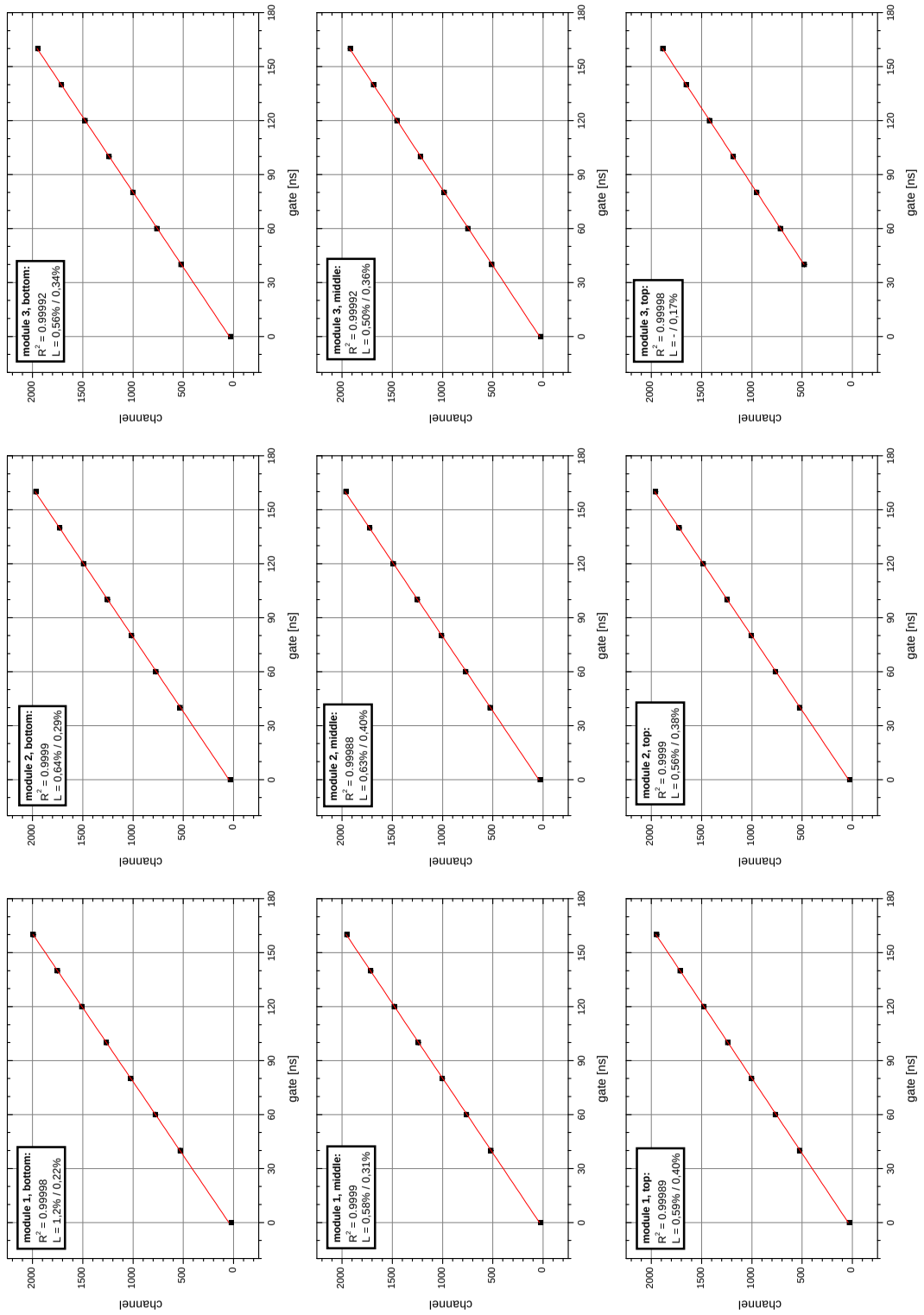

Figure 5.2: Measurement of the non-linearity L of 9 ADCs. The amount of charge on the ADC inputs was controlled using a rectangular gate of several nanoseconds width. The first L-value includes the lowest measured point, the second ignores it.

5.2 Advantages of VME

All previous experiments with the spectrometer *PERKEO II* used the CAMAC[1] system for the computer based data acquisition. One part of this thesis was to change the electronics to VME[2]. A short comparison between the systems can be found in [Mun00].

In this section, we just want to focus on the advantages of VME that were the reasons for the change: The most important advantage is that our VME modules are not interrupt controlled as the CAMAC system. We have FIFO[3] memory chips on the modules (except on the scalers and the digital IO) that store the data if an event occurs. This is much faster than producing an interrupt and processing it immediately with the computer, hence we can effectively reduce the dead time of the measuring system (see chapter 5.4).

This benefit brings along a weak point: One event consists of several information parts, e.g. energy and time, that are written into the FIFOs of different modules. We read all data from the memories when the spin is flipped whereas we have to ensure that the number of entries in all FIFOs is exactly the same. If we lose just one event in one device we cannot use any of the data since we do not know which of the events is incomplete.

When we look into the future, another advantage of the SIS3100 (SIS GmbH) VME system is its block transfer feature: Since we expect count rates (including background) of 600 Hz we do not need the fast block transfer at the moment, but the *New PERKEO*, the successor of our spectrometer, is already in the planning phase [Dub03]. This istrument will use a pulsed neutron beam and achieve one order of magnitude higher peak count rates and will have to use fast data transfer capabilities [Mae03].

5.3 The Program VME-MOPS

`VME-MOPS`, the Measuring and Operating System for the *PERKEO*-experiment, is a program that performs the measurements, i.e. it reads out the modules in certain time intervals, and controls the experiment by enabling the spinflipper, moving the shutters and inserting radioactive calibration sources into the spectrometer.

The program package consists of three individual programs: `MOPS` that communicates directly with the electronics modules, `GRAMOPS`, a graphical interface for `MOPS`, and `ROOTMOPS` that displays the measured spectra. Originally, all programs were written by M. Brehm [Bre03].

We did not change anything in `ROOTMOPS` and undertook just some slight improvements in `GRAMOPS`, but we had to change the old `MOPS`, which was a realtime CAMAC version,

[1] CAMAC: Computer Aided Measurement And Control
[2] VME: Versa Module Euro card
[3] FIFO: First In, First Out; the oldest datum is read first

to VME-MOPS that is able to operate the VME technology. Hence we have rewritten the program just maintaining the communication routines with the other two programs.

The basic innovation is the use of the onboard FIFOs of the VME-modules: The measuring time between two spinflips is 10 seconds and during this time only the TDC, whose FIFO is very small, is read out on a regular basis without interrupting the measurement. VME-MOPS reads out all other memories and scalers when the spinflipper status changes. During this procedure, we have to wait for two seconds anyway to ensure that the flipper is working properly. In this way we are able to reduce the dead time of the detector system dramatically (chapter 5.4).

VME-MOPS has the following features:

- Reading electron events (a event consists of 8 ADC values, one or more TDC values, one latch pattern and one global time).
- Writing events in binary files; the events can also be written into ASCII spectra to work with the data immediately.
- Writing a binary protocol file for each eventfile including scaler values (total time, dead time, ready time, conincidences, electron gates, neutrons), filename, shutter positions, calibration sources, spinflipper status, date and time.
- Writing an ASCII-logfile with the same information for all eventfiles; the error messages are also written to the logfile.
- VME-MOPS is controlled by GRAMOPS and the spectra are displayed in ROOTMOPS.
- A global eventcounter is implemented (i.e. a number is assigned to each event).
- The spinflipper is controlled using the digital IO.
- The three shutters (shutter up is placed in front of and shutter down behind the collimation system, the beamstop shutter is placed directly in front of the beamstop), the calibration sources and the YZ-Scanner are controlled by VME-MOPS using external programs.

Besides some minor improvements, the overall principle of MOPS was not changed, hence its mode of operation and how the measurements are performed can be found in older theses, e.g. [Ast97] and [Mun00]. In the next two sections, we will focus on two newly implemented features:

5.3.1 Event Time Information

For the first time we added a time counter with FIFO to the electronics system to monitor the chronology of the events. Now we are able to detect "wrong" periodic signals that occur more than one dead time after the preceding event. Signals occurring within the first 200 ns are detected within the ADC gate time using the normal TDC and signals that arise within the conversion time of the detector system cannot even enter the data acquisition system since it is disabled.

The new device was build by the electronics laboratory of the Physics Institute Heidelberg and contains a clock that is started with an external gate. When the time counter is enabled and a trigger signal occurs due to an event, the current counter value is shifted to the FIFO. In this way we are able to assign a global time value to each registered event and can identify potential wrong events by the time interval to the preceding signal.

5.3.2 Background Monitors

The A-measurement will be performed in the big neutron guide hall at the ILL. Many experiments housed in this building change their setup on an hourly basis so that the overall background in the hall may be variable with time. This effect was reported by the *Trine*-experiment [Sol03].

To monitor this background and its influence on our measurements, we will install two plastic scintillators next to the two detectors but outside the vacuum system. The scintillators are attached to photomultipliers whose signals are discriminated and counted by scalers. These numbers are written to the event files like all the other scaler values.

5.4 Dead Time

The dead time of a detector system is the finite time required to process a signal [Leo94]. It has a direct influence on the A-measurement since an electron event occurring during the dead time interval will not be detected and will therefore change the asymmetry.

We measured the dead time of the new VME data acquisition system using a NIM-clock as input signal. It was used for the analog branch as well as for the logic branch. Another 1 MHz clock was counted by the total time scaler. When a busy output of a VME-ADC (that has the longest conversion time) was high, the 1 MHz clock signal was additionally transferred to a dead time counter. Comparing the number of events, the total time and the dead time yields the dead time per event of the detector system. We obtained a dead time of $\Delta t = (1.79 \pm 0.03)$ μs/event where the error is only statistical.

This value is more that 20 times lower than the dead time of the realtime CAMAC `MOPS` (44 μs [Bre03]) and about 60 times lower than at the last A-measurement (112 μs [Mue96]).

The rate R that is lost by the finite dead time can be estimated by

$$R = r^2 \cdot \Delta t, \tag{5.2}$$

where r is the expected event count rate and Δt the dead time. Combining an assumed rate $r = 400$ Hz and the measured dead time, we obtain $R \approx 0.29$ Hz corresponding to a $7 \cdot 10^{-4}$ effect.

5.5 Tests

Tests with the electronics setup were performed in Heidelberg without vacuum and without magnetic field. We used a $50 \times 50 \times 5$ mm^3 BICRON 404 plastic scintillator attached to a HAMAMATSU mesh photomultiplier tube with vacuum grease. A ^{207}Bi source was placed directly on the scintillator. We multiplied the signal with a linear FAN and put it to the inputs of all 8 ADCs. A typical spectrum is shown in figure 5.3; the lower peak can be hardly seen due to the high background and because neither gain nor offset of the ADCs were optimized for the tests.

The new data acquisition system is sufficient for count rates up to 720 Hz if the time of one cycle (10 s) should not be decreased. For the real experiment, we expect an electron event rate of approximately 400 Hz (see chapter 6.2.4) and a signal to background ratio better than 2:1, since this was the ratio of the last A-measurements and we want to reduce the background. Hence the effective count rate will be around 600 Hz what can be handled by `VME-MOPS` without problems.

We also made long time tests of the electronics setup: `VME-MOPS` worked uninterrupted more than 145 hours without the occurrence of any error. Therefore we expect no problems for the experiment, where the measurement will be interrupted and the data saved to CD at least once a day.

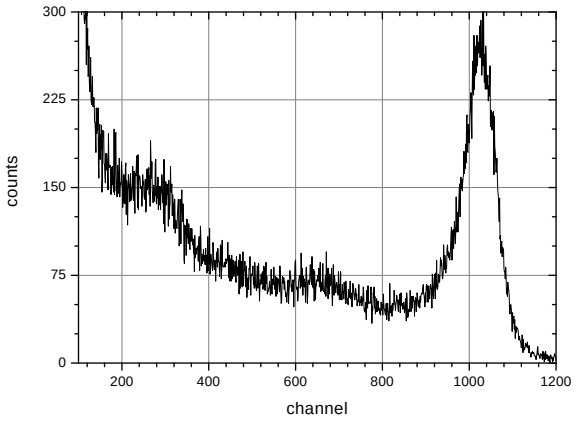

Figure 5.3: `VME-MOPS` test measurement: The ^{207}Bi-spectra were obtained with a $50 \times 50 \times 5$ mm^3 plastic scintillator attached to a photomultiplier tube. We used a linear FAN to put the signal on all 8 ADC inputs. The lower peak can be hardly seen due to the high γ-background.

Chapter 6

The first Beamtime

In this chapter, we present the results of the first part of the *PERKEO II* beamtime performed at the cold neutron beam place PF1b of the Institut Laue-Langevin (ILL) in fall 2003. The aims for the 25 days of beamtime were the following:

- Installation of the beamline and the collimation system.
- Build-up of the polarization setup to produce a highly polarized beam with a wavelength-independent polarization.
- Measurement of the beam properties like flux, beam profile and wavelength spectrum.
- Analysis of the beam polarization using two complementary methods: The relative method uses supermirror polarizers to analyze the beam. It allows the determination of the spinflip efficiency $\mathcal{F}$ and of the products AP and $AP\mathcal{F}$, where A is the analyzing efficiency and P the degree of polarization. Taking the square root of AP gives a good approximation of the polarization.

  The absolute method uses polarized ^{3}He as analyzer. The analyzing efficiency is known to be $A = 100$ % in the maximum and we are able to obtain an absolute value for the polarization P.

We will discuss these topics in detail in the following sections.

6.1 The Radiofrequency Spinflipper

This is the first time that the *PERKEO II*-experiment uses a radiofrequency spinflipper [Baz93], therefore we will shortly describe its functionality:

We need a spinflipper to reverse the neutron spin by 180° to measure the polarization (chapter 6.3) and to determine systematic effects due to inhomogenities of the beam and

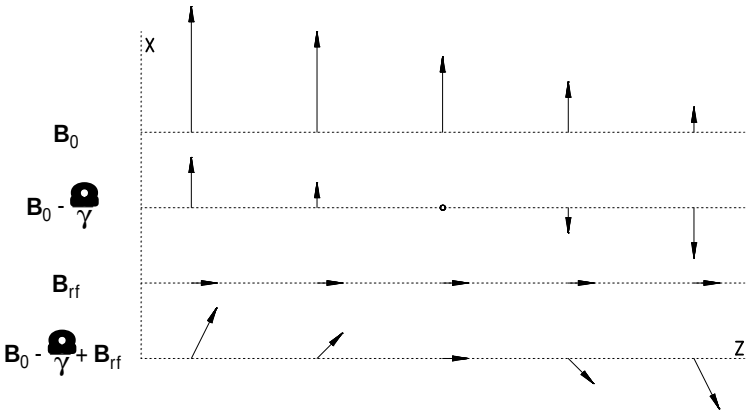

Figure 6.1: The magnetic fields of the resonance spinflipper: $\mathbf{B}_0$ is the static field in the laboratory frame; it changes to $\mathbf{B}_0 - \frac{\Omega}{\gamma}$ if it is transformed to the frame of the neutron, rotating with Ω. In this frame $\mathbf{B}_{rf}$ is constant. Therefore the effective field $\mathbf{B}_0 - \frac{\Omega}{\gamma} + \mathbf{B}_{rf}$ rotates the spin. (Figure taken from [Bre03].)

the magnetic field. During the last runs, this was achieved using a current sheet spinflipper, but this device works only well for fast neutrons and produces background radiation since it requires a sheet of matter within the beam. Additionally, it is impossible to install a guiding field around the current sheet spin flipper what may cause depolarization. It is also very difficult to place it inside the vacuum system due to its large dimensions.

A radiofrequency spinflipper does not have these disadvantages: It consists of a radiofrequency (rf) coil centered in an orthogonal static magnetic field with a field gradient; the neutrons can pass the rf-coil without interacting with matter. In our case, the coil is evacuated and part of the beamline. Moreover, its flipper efficiency, beyond a certain threshold wavelength, is independent from the neutron wavelength and close to unity.

In the laboratory frame, the effective field of the rf-spinflipper is a superposition of the static field orthogonal to the beam direction and the time variable parallel field, oscillating with the Larmor frequency

$$\Omega = \frac{2}{\hbar}\,\mu_n \mu_B B_0 = \gamma B_0 = -1.832 \cdot 10^8\ B_0\ \frac{\mathrm{rad}}{\mathrm{sT}}, \tag{6.1}$$

where $\mu_n = -1.913$ is the magnetic moment of the neutron, μ_B the Bohr magneton and B_0 a value of the static field at some point close to the center of the coil. In the reference frame of a neutron rotating with Ω, the osciallating field B_{rf} is constant whereas the static field becomes variable in time. In this frame the superposition of the transformed fields causes a rotation of the effective field by 180° and the neutron spin is also turned if the adiabatic condition is not violated (see figure 6.1). In the laboratory frame the effective field is not rotated, but the neutron leaves the rf-coil with its spin reversed.

The disadvantage of the radiofrequency spinflipper is that it may emit the radiofrequency, causing interferences with electronic devices.

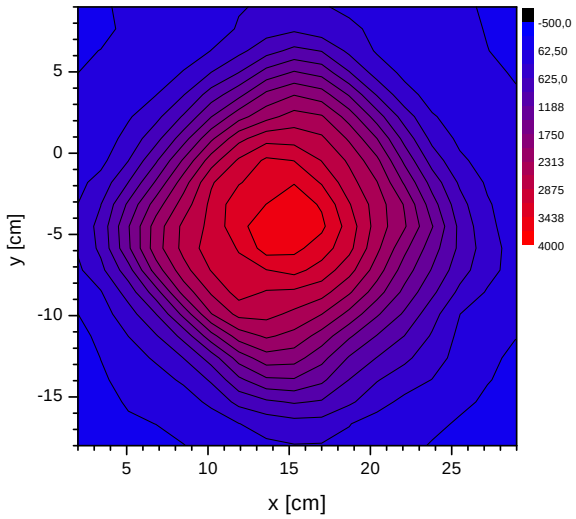

Figure 6.2: Beam profile behind a pinhole diaphragm, measured at the end of the experimental zone.

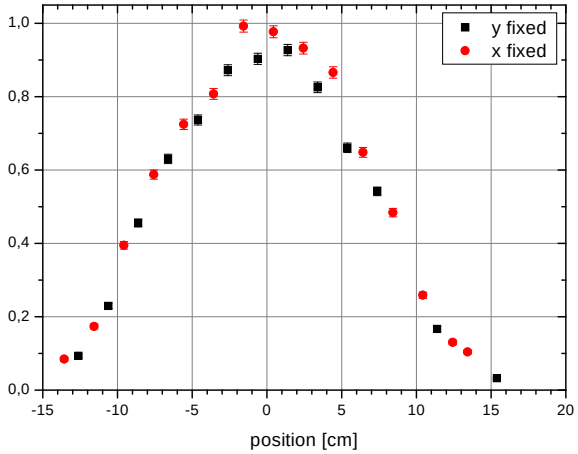

Figure 6.3: Cuts through the beam center of figure 6.2. It is almost Gauss-shaped and shows a clear maximum.

6.2 The Beam

In this section we describe the properties of the polarized neutron beam as it leaves the PF1b concrete casemate. In the casemate, the polarizers are installed inside a lead channel to shield the sensitive detectors from the gamma background produced during the polarization process.

6.2.1 Beam Profile behind the Polarizers

We determined the straight neutron beam using a pinhole diaphragm ($\emptyset = 3$ mm) directly attached behind the second polarizer and a helium detector with a sensitive area of 20×20 mm located at the end of the experimental zone (≈ 9 m behind diaphragm; figure 6.2) and at the position of the decay volume (≈ 5 m; figure 6.4). It was possible to move the detector in x and y-direction to obtain the beam profile at the two distances.

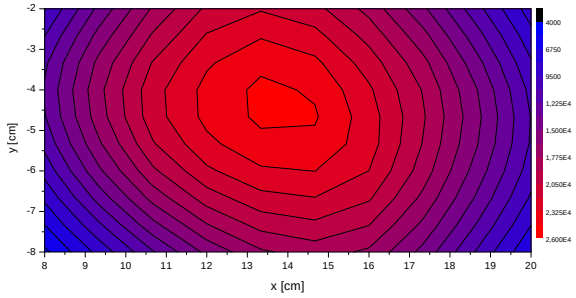

Figure 6.4: Beam profile behind a pinhole diaphragm, measured at the position of the *PERKEO II* decay volume. As in figure 6.2, the x- and y-coordinates are relative positions.

To reduce the beam intensity we performed the measurement with two 4 mm plexiglass attenuators placed between the polarizers. These reduce the intensity by scattering but also cause a slight change in the wavelength spectrum. Since the neutron angles depend on the wavelength, the measured beam profiles are not identical to the profiles of the unattenuated beam. We obtained the beam center from figure 6.3 and marked the beam direction with a laser pointing towards the polarizer.

6.2.2 Beamline and Collimation System

Build-up of the Beamline: When we had obtained the direction of the straight beam and the laser installed we were able to assemble the beamline: It consists of a spinflipper, a corrugated tube, two T-pieces and a one meter beam tube with a T-opening for the shutter down (see figure 3.1). The alignment of the diaphragms and the tubes was determined using a theodolite[1] positioned in the straight beam and copper foil images (chapter 6.2.3). We put tubes out of glass and lithium rubber into the beamline to absorb neutrons scattered by the diaphragms.

Outside the beam line we installed a magnetic guiding field ($B \approx 1.3$ mT) perpendicular to the beam to prevent depolarization of the neutrons.

The "real" Collimation System: We made the diaphragms a little bit smaller than recommended in chapter 3 to avoid that the direct beam can hit the lithium rubber inside the diaphragm openings, what increases the number of scattered neutrons. Therefore, we obtain a decreased electron count rate of (481 ± 22) Hz when we use the program `MCstrahl` to simulate the current collimation system. We also used a reduced capture flux $\phi_c = 1.6 \cdot 10^9$ cm^{-2} s^{-1}, which was measured with gold foil activation (chapter 6.2.4). The size and position of the diaphragms can be found in the following table:

	distance [cm]	x [mm]	y [mm]	neutrons [%]	fast n [kHz]
polarizer diaphragm	0	58.0	37.5	56.42 ± 0.09	4076
diaphragm −1	22	51.0	42.0	5.56 ± 0.02	405
diaphragm 0	39	42.5	30.5	12.58 ± 0.04	913
diaphragm 1	134	33.3	22.3	13.55 ± 0.04	978
diaphragm 2	214	31.7	18.3	5.09 ± 0.02	338
diaphragm 3	267	32.3	18.9	1.37 ± 0.01	84
decay volume	517	126.2	80.0	5.44 ± 0.02	-
beamstop	935	-	-	5.44 ± 0.02	3711
count rate: (481 ± 22) Hz		(Flux: $1.6 \cdot 10^9$ cm^{-2} s^{-1})			

[1] A theodolite is a telescope with crosshairs.

Diaphragm -1 is an additionally diaphragm that does not shape the beam geometrically. It is placed between the polarizer diaphragm and diaphragm 0 and is build out of a 110 mm thick lead base to shield the gamma radiation produced by the polarizers. The front of the diaphragm is covered with ^{6}LiF-tiles and its inside and back plane are protected with lithium rubber.

To prevent neutrons scattered from the diaphragms from hitting the detector region, we have installed two halo diaphragms between the downstream shutter and the decay volume. But these are large enough not to interfere with the direct beam.

6.2.3 Copper Activation Analysis

We can obtain images of the neutron beam profile using the activation of a copper foil by the neutron beam: ^{63}Cu (69 % natural abundance) is transmuted to ^{64}Cu due to neutron capture just as ^{65}Cu (31 % natural abundance) is transmuted to ^{66}Cu. The latter has a half of $t_{1/2} = 5.1$ min, producing a fast radiation component. To avoid temporal effects, one should wait until this component is decayed. Then the activated copper foil is put on an image plate that is transferred into a metastable excited state under irradiation. We read out the image plate with a special scanner and get a black and white image of the beam, which was used to ensure that the diaphragms were perfectly adjusted to the beam maximum.

Cu-foil images were taken at several points of the setup to check that the beam maximum is centered in the beamline: At the entrance window of the second polarizer (figure 6.5), behind the second polarizer to determine size and position of the polarizer diaphragm (figure 6.6). Moreover, we obtained images behind the spinflipper, behind diaphragm 1 (figures 6.7, 6.8), behind diaphragm 2, and behind diaphragm 3. All images show an almost symmetric beam profile with a slighly steeper drop-off at the left side (seen in reactor direction) which is probably due to the curved neutron guide. The small asymmetry is not critical, since the A-measurement performed with two opposing detectors is insensitive to the beam profile.

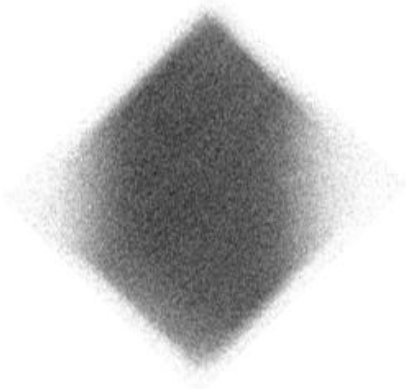

Figure 6.5: Cu-foil image of the neutron beam at the entrance of the second polarizer to ensure that the beam propagates correctly through the polarization setup. In all images on this page, the neutrons propagate out of the plane.

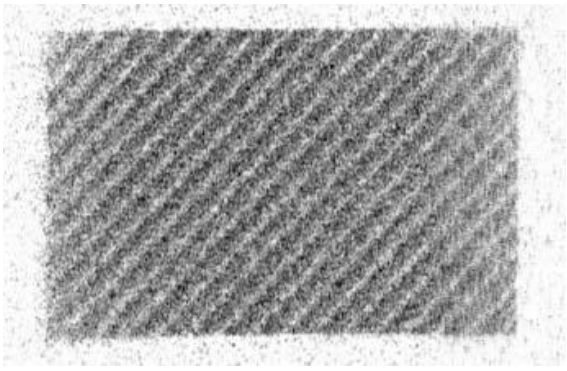

Figure 6.6: This image of the beam behind the polarizer diaphragm was used to determine its position: The beam is constant over the diaphragm center and decreases slightly at the edges. The stripes are due to the individual mirrors of the polarizer.

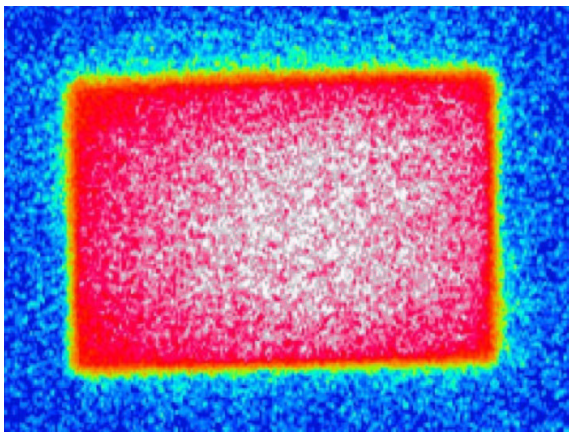

Figure 6.7: Miscolored Cu-foil image obtained behind diaphragm 1 (the neutrons propagate out of the plane).

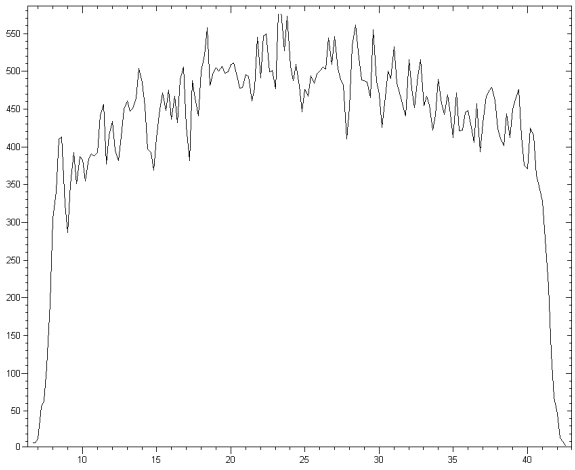

Figure 6.8: Horizontal cut through the center of figure 6.7. The x-axis is given in mm, the y-axis in arbitrary units. The graph shows an almost symmetric beam profile with the maximum at the center. The decline to 70 % is slightly steeper on the left side.
The simulated beam profile in figure 3.7 only declines to 78 %, thus the neutron distribution on the polarizer is not as homogenious as assumed in the simulation.

6.2.4 Flux Measurements

Mass-calibrated pieces of gold foil activated several minutes by the full neutron beam are used to obtain the capture flux ϕ_c since gold has a $\frac{1}{v}$-cross section for neutron capture. One measurement plate consists of five evenly distributed gold foils with 1 cm diameter to get an average flux value for the whole beam. We made gold foil activations at several positions (the 5 % error is given by the systematics of the measurement):

position	ϕ_c [n cm^{-2} s^{-1}]
behind neutron guide	$(13.3 \pm 0.7) \cdot 10^9$
behind the first polarizer	$(3.40 \pm 0.17) \cdot 10^9$
behind the second polarizer	$(1.63 \pm 0.08) \cdot 10^9$
behind diaphragm 3	$(4.36 \pm 0.22) \cdot 10^8$

Since all neutrons that pass the last diaphragm will also propagate through the decay volume, we can use the capture flux $\phi_c = 4.36 \cdot 10^8$ n cm^{-2} s^{-1} to estimate the number of neutrons decaying inside the spectrometer: Diaphragm 3 has an area of $a = 3.23 \times 1.89$ cm^2, the decay volume is $L = 27$ cm long and the number of decaying neutrons is given by

$$n \approx \frac{\phi_c a L}{v_{therm} \tau} = 369 \text{ Hz}, \tag{6.2}$$

where $v_{therm} = 2200$ m s^{-1} is the thermal velocity and $\tau = 886$ s the neutron lifetime.

This number is 23 % lower than expected by the simulation of the setup, which is most likely due to the imprecise angular distribution of the neutrons in the program. But we made the measurements with a reduced reactor power of 54 MW (instead of 58 MW as usual; 7 % loss) and we neither did rinse the polarizers with helium nor measured with an evacuated beamline (and therefore had scattering losses). Hence we expect the event rate to be at least 10 % higher during the experiment.

6.2.5 The Wavelength Spectrum

To measure the wavelength spectrum of the full neutron beam behind the last diaphragm (beamline evacuated) we constructed a time-of-flight (TOF) setup: It consists of a chopper with four slits running at a slit-frequency $\nu \approx 50$ Hz and a $\frac{1}{v}$-He-detector (efficiency 10^{-6}) at a distance of about 1.60 m. A photo sensor always starts the measurement when a chopper slit is open and a bunch of neutrons propagates towards the detector. We determine the time of flight for each detected neutron. This is a direct measurement of the $\frac{1}{v}$-weighted wavelength spectrum, which is shown in figure 6.9.

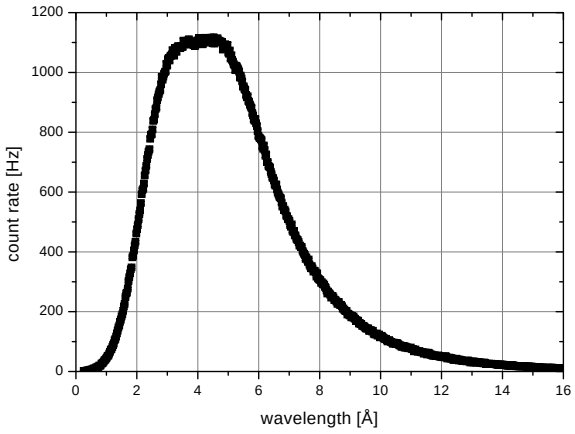

Figure 6.9: $\frac{1}{v}$-weighted wavelength spectrum of the beam behind the last diaphragm. The spectrum is corrected for dead time effects and the chopper offset.

6.3 Polarization

In this section, we present the installations and measurements concerning the polarization of the neutron beam. To start with, we will shortly summarize some facts about neutron polarization:

Polarizing a Neutron Beam: A neutron beam is called polarized if a certain fraction of the spins is aligned to a specific direction **a**. The spin polarization can be treated as a classical vector in the laboratory frame [NDB02]. When $N^{\uparrow}$ is the number of neutrons with spin eigenstate $+\frac{1}{2}$ and $N^{\downarrow}$ corresponds to the state $-\frac{1}{2}$, the polarization in the direction **a** is defined by

$$P_{\mathbf{a}} = \frac{N^{\uparrow} - N^{\downarrow}}{N^{\uparrow} + N^{\downarrow}}. \tag{6.3}$$

We use supermirror[2] polarizers to polarize the beam. These exploit the fact that the reflection on the magnetic potential of some magnetic materials depends strongly on the relative orientation between the neutron spin and the magnetic field in the material. The materials can be assembled in a way that one spin component, hitting the mirror at small angles, transits the magnetic layers and is finally absorbed, whereas the other spin component is reflected by Bragg-reflection. Since the polarizer consists of several curved mirrors, each neutron is at least reflected once, therefore the beam behind the polarizer is polarized.

To increase the polarization, we use two successive supermirror polarizers that are independent from each other since the second is rotated by 90°. The latter additionally polarizes the beam in the orthogonal direction yielding a high degree of polarization, which is constant over a wide wavelength range. This "crossed geometry setup" is described in [Pet02] and [Bre03]. Since supermirror polarizers deflect the neutron beam by a small angle, we

[2]Total reflection of neutrons on solid state surfaces only occurs when the momentum perpendicular to the surface is smaller than a certain critical value p_c, corresponding to a maximal incident angle Θ (critical angle). Supermirrors use several layers of different materials to enlarge this angle [Sch89].

have to turn the whole polarizing setup by 45°, because we need a horizontal beam to perform the measurements with *PERKEO II*. Now the polarized beam is vertically shifted and horizontally deflected compared to the incident neutron direction.

6.3.1 The new Polarizer

For the first time, an A-measurement with *PERKEO II* will use two polarizers in the crossed geometry setup mentioned above. Therefor a new polarizer was assembled in Munich (Technische Universität) and at the ILL.

This supermirror polarizer ($m = 2.8$), which will be used as the second polarizer in the crossed geometry setup, is constructed in the same way as the one used at PF1b during the *Trine* experiment, which was the predecessor of *PERKEO II* at the ILL. Therefore the characteristics of the old polarizer are well known [Sol02] and we only had to check the new one. To do so, we used a setup build out of the *Trine* polarizer (polarizing efficiency P), the *Trine* radiofrequency spinflipper (spinflip efficiency $\mathcal{F}$) and the new polarizer used as analyzer (analyzing power A).

Angular Characteristics of the new Polarizer: We obtain the incident angle α for maximal neutron transmission by turning the new polarizer behind a slit diaphragm. The result is ($\alpha = 11.6 \pm 1.0$) mrad where the error is purely systematical. Since the incident neutron beam is polarized by the "old" polarizer and transits the spinflipper afterwards, we can determine the spinflip ratio, a measure for the polarizing power. It is 61.7 ± 1.4, which is quite reasonable for an untuned system.

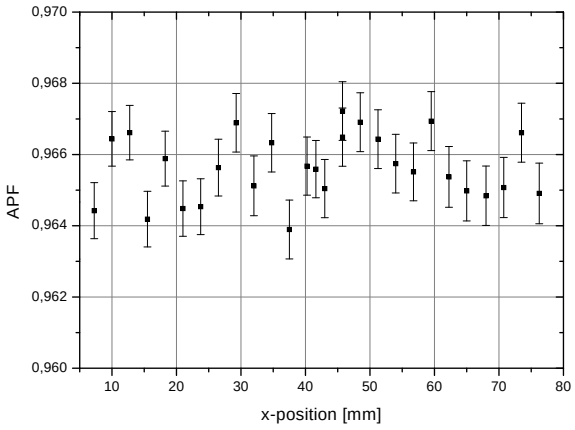

Figure 6.10: The polarization AP of the lower part of the new polarizer shows no spatial dependence.

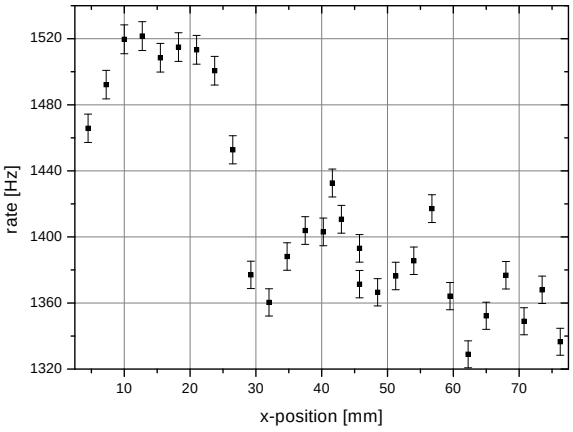

Figure 6.11: The transmission of the new polarizer decreases by approximately 15 % from the left to the right (seen in reactor-/negative-z-direction).

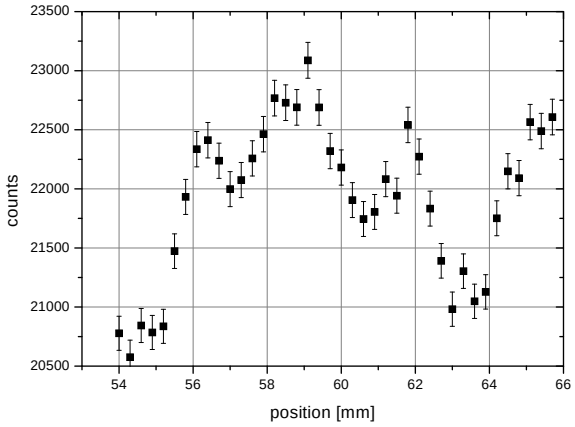

Figure 6.12: The transmission of the new polarizer measured with a 1 mm slit diaphragm: The little peaks stem from the individual supermirrors, which are separated by 2.8 mm. Where the neutrons hit the mirror body the transmission decreases.
The position is a relative measurement and not identical with the scale on figures 6.10 and 6.11.

Spatial Characteristics: We scanned the polarizer horizontally using a 5 mm slit diaphragm at its entrance to determine the spatial dependence of polarization and transmission. The results are shown in figure 6.10 and 6.11: In the polarizer-spinflipper-analyzer setup, we can only measure the product $AP\mathcal{F}$. Assuming $\mathcal{F} \approx 1$ and $A = P$ allows us to estimate A; we obtain $A \approx \sqrt{AP} = 98.3$ % averaged over all wavelengths, which is quite good for an unoptimized system. (A for the older polarizers build by O. Schärpf is $A = 97.5$ % [Ser98].) But much more important is the fact that the polarization is constant over the whole polarizer window.

This is not the case for the transmission, which drops by 15 % from the left to the right (seen in reactor direction) and shows some structures in the plot. Since the polarizer consists of 30 supermirrors, this effect is likely due to inaccuracies in the assembly or due to differences in the mirrors. A similar behaviour has previously been observed with other supermirror polarizers. We can directly see the single mirrors using a narrower diaphragm opening (1 mm; figure 6.12).

All figures shown here, polarization and transmission, were obtained using only the lower part of the new polarizer, but we checked that the upper part behaves equally.

6.3.2 Adjustment of the Crossed Geometry Setup

To arrange the two polarizers efficiently in a crossed geometry turned by 45°, the mechanical workshop of the Physics Institute, Heidelberg, designed a special adjustment device (figure 6.13). It allows to move the polarizers independently in two perpendicular planes. Moreover one can change position and height of the individual mountings to guide the neutron beam through both polarizers.

Figure 6.13: The device to arrange the polarizers in crossed geometry. The whole setup is rotated by 45° to obtain a horizontal neutron beam. We place the polarizers in the V-shaped mountings and position them individually using the adjusting screws at the front and the back.

The adjustment procedure is the following:

- Exploit the measured geometric characteristics of the two polarizers for a rough preadjustment of the whole setup.
- Adjust the first polarizer to maximal transmission.
- If the first polarizer is inclined by an angle x, the second polarizer must be inclined by $2x$ in the same plane.
- Position the second polarizer such that the beam hits the polarizer center.
- Adjust the second polarizer to maximal transmission in the orthogonal plane.
- Check if the beam is horizontal and readjust the second polarizer where applicable. This can be done because transmission and polarization are rather insensitive to small changes in the angle.

Since the second polarizer is turned by 90° with respect to the first, the neutron spin has to be rotated between the polarizers, too. We achieve this by using an appropriate magnetic guiding field.

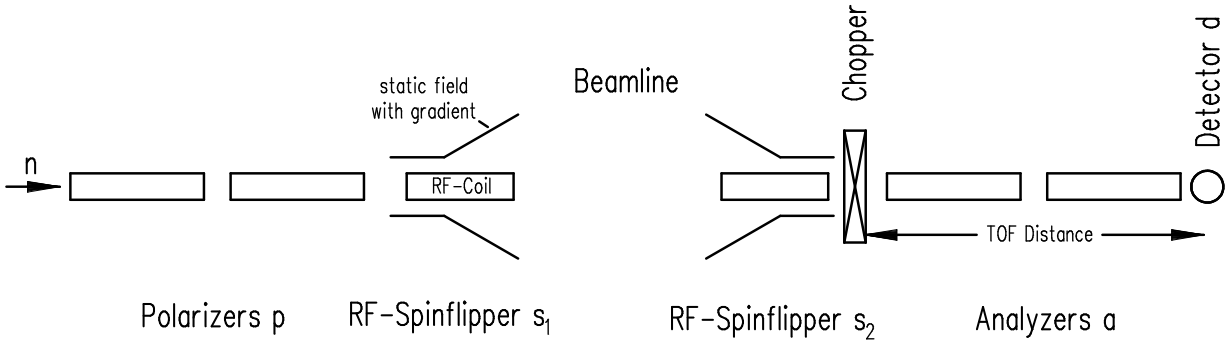

Figure 6.14: The experimental setup for the relative polarization measurement and the determination of the spinflip efficiency.

6.3.3 Polarization Measurements

Since the polarization P directly enters the experimental asymmetry A_{exp}, formula (2.30)[3], it is crucial for the next run of *PERKEO II* that the neutron beam is highly polarized and, what is even more important, that the polarization is known to a very high degree.

We measured the polarization at the distance of the decay volume before spectrometer and steel shielding were placed in the experimental zone. This has never been done before; the polarization was always measured behind *PERKEO II* with its strong magnetic field. Now we can check for potential depolarization effects inside the spectrometer by comparing the data presented in this chapter with polarization measurements behind the decay volume that will be performed in spring 2004.

6.3.3.1 Relative Measurement

We used the setup shown in figure 6.14 for the relative measurement of the polarization: The beam is polarized with two crossed polarizers, passes two rf-spinflippers, transits a chopper, gets again polarized in two crossed analyzers and is finally detected with a He-counter. This setup allows us to determine the parameters of the devices:

Mathematical Description of the Measurement: Classical two-component vectors are sufficient to describe the polarization of a neutron beam in an external field. The unpolarized beam is given by

$$\mathbf{n} = n_0 \begin{pmatrix} 1 \\ 1 \end{pmatrix}. \tag{6.4}$$

If the polarizer $\mathbf{p}$ has the polarizing power P and the analyzer $\mathbf{a}$ the analyzing power A and we assume no depolarization in the polarizers, the devices can be described by the

[3]Note that the factor A in this formula is the electron asymmetry and not an analyzing power.

matrices

$$\mathbf{p} = \begin{pmatrix} 1+P & 0 \\ 0 & 1-P \end{pmatrix} \quad \text{and} \quad \mathbf{a} = \begin{pmatrix} 1+A & 0 \\ 0 & 1-A \end{pmatrix}. \tag{6.5}$$

A spinflipper $\mathbf{s}$ with the efficiency $\mathcal{F}$ is represented by

$$\mathbf{s} = \begin{pmatrix} 1-\mathcal{F} & \mathcal{F} \\ \mathcal{F} & 1-\mathcal{F} \end{pmatrix}. \tag{6.6}$$

Since the detection in the He-counter is spin-independent we describe the detector $\mathbf{d}$ with the efficiency ϵ using the vector

$$\mathbf{d} = (\ \epsilon \quad \epsilon\ ). \tag{6.7}$$

We apply these representations to calculate the detector count rate after an arbitrary combination of the devices. With our setup we can measure the rates N_{ij} where $i(j) = 1/0$ indicates whether the first (second) spinflipper is active/inactive:

$$\begin{aligned} N_{00} &= \mathbf{d\ a\ p\ n} & N_{10} &= \mathbf{d\ a\ s}_1\ \mathbf{p\ n} \\ N_{01} &= \mathbf{d\ a\ s}_2\ \mathbf{p\ n} & N_{11} &= \mathbf{d\ a\ s}_1\ \mathbf{s}_2\ \mathbf{p\ n}. \end{aligned} \tag{6.8}$$

Combining the count rates we can calculate the device parameters that we are interested in, e.g. the efficiency

$$\mathcal{F}_1 = \frac{N_{11} - N_{10}}{N_{00} - N_{01}} \tag{6.9}$$

of the first spinflipper or the product

$$AP\mathcal{F}_1 = \frac{N_{00} - N_{10}}{N_{00} + N_{10}}, \tag{6.10}$$

which is independent of the second spinflipper. However, it is impossible to obtain solely P with this method; that is why it is called "relative": We can only get rid of the flipper efficiencies $\mathcal{F}_1$ and $\mathcal{F}_2$ and measure the product AP:

$$AP = \frac{(N_{00} - N_{10})(N_{00} - N_{01})}{N_{00}N_{11} - N_{01}N_{10}}. \tag{6.11}$$

Taking the square root of AP gives a good approximation for the polarization P, which assumes that the polarizer and the analyzer are comparable.

Results: We obtained the spinflip efficiency $\mathcal{F} \equiv \mathcal{F}_1$ of the new *PERKEO II* radiofrequency spinflipper from measurements of N_{11}, N_{10}, N_{01} and N_{00} applying formula (6.9). The mean flipper efficiency in the region of interest between 2 and 12 Å (this is the wavelength region where we can measure the relative polarization with high precision) is $\mathcal{F} = 1.0002 \pm 0.0008$ and can therefore be set to unity (figure 6.15).

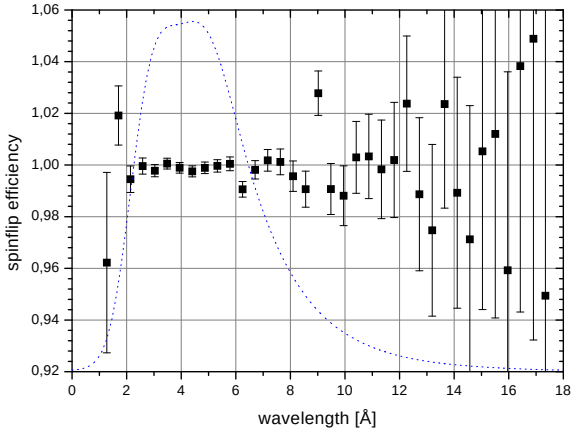

Figure 6.15: The efficiency $\mathcal{F}$ of the *PERKEO II* radiofrequency spinflipper (flipper s_1 in the setup). Its mean value between 2 and 12 Å is $\overline{\mathcal{F}} = 1.0002 \pm 0.0008$ hence we can set it to unity. The dottet curve indicates the spectrum of the neutron beam measured in the beam center.

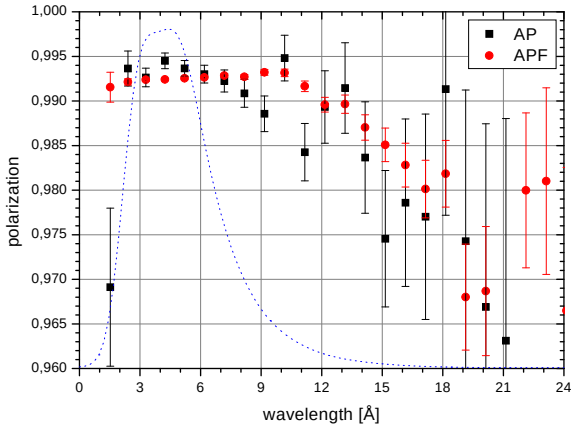

Figure 6.16: The polarization measured in the beam center. We cannot use AP for the polarization analysis due to unphysical structures in the curve, caused by interferences between the second rf-spinflipper and the detector. In contrast to this $AP\mathcal{F}$, which is determined using only the first spinflipper, is flat.

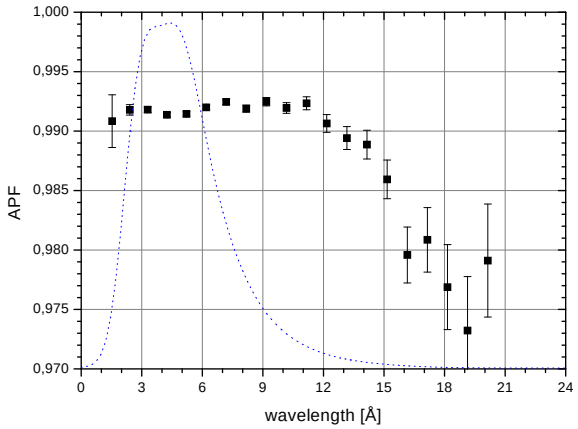

Figure 6.17: $AP\mathcal{F}$ measured with supermirror analyzers 15 mm left of the beam center.

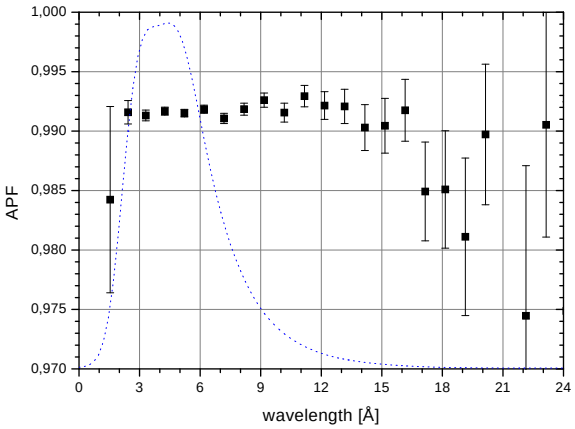

Figure 6.18: $AP\mathcal{F}$ measured with supermirror analyzers 15 mm right of the beam center.

Unfortunately this measurement was the only one where we could use both spinflippers. When we tried to optimize the configuration of the second spinflipper, we got structures in the spinflip efficiencies, caused by interference between the second spinflipper and the detector. This yielded values greater than one in $\mathcal{F}$ and unphysical structures in AP, which is shown in figure 6.16. Hence we can only work with $AP\mathcal{F}$ whose determination is independent of N_{11} (equation 6.10). However, this is no problem for the analysis since we know that $\mathcal{F} \approx 1$.

We measured the polarization in decay volume distance at three horizontal positions: in the beam center and 15 mm left and right of this point. The results corrected due to background and deadtime are presented in the figures 6.16-6.18. They show a flat polarization $AP\mathcal{F}$ in the range from 2 to 12 Å and a decrease for higher wavelengths where the measurements suffer from low statistics. We can make no statement on the polarisation for small wavelengths. The statistical accuracy for the points between 2 and 12 Å is better than 10^{-3}.

We have to weight the polarization with the neutron spectrum to obtain mean values $\overline{AP\mathcal{F}}$ for the three positions. Taking the square root of this number gives a good approximation for P, assuming that $A \approx P$. The results for wavelengths between 2 and 12 Å are summarized in the following table, where the error is purely statistical:

position	$\overline{AP\mathcal{F}}$	$P > \sqrt{\overline{AP\mathcal{F}}}$
15 mm left	0.9918 ± 0.0001	0.9959 ± 0.0001
beam center	0.9925 ± 0.0001	0.9962 ± 0.0001
15 mm right	0.9916 ± 0.0002	0.9958 ± 0.0001

The mean values for the whole spectrum (0-25 Å) are only slightly lower (~ 0.01 %) due to the strong suppression of neutrons with large and small wavelengths in the convolution with the wavelength spectrum.

6.3.3.2 Absolute Measurement with Helium Cells

To determine the absolute polarization P from the relative measurement of AP we have to know the analyzing power A exactly at least at one wavelength. This is the case if we use polarized ^{3}He to analyze the beam [Zim99]:

Polarized ^{3}He can be used as an opaque spin filter for a certain wavelength range: It is only transparent for neutrons that have their spin parallel to the nuclear spin due to the strongly spin-dependent absorption cross section. If a cell with polarized ^{3}He is put into an unpolarized neutron beam it removes the neutrons with anti-parallel spins efficiently and hence polarizes the beam.

The disadvantage of helium cells, besides the ongoing nuclear spin relaxation, is that the absorption cross section depends strongly on the wavelength since it is proportional to $\frac{1}{v}$.

Hence we need several cells with different gas pressures and sizes to analyze the whole spectrum.

The wavelength-dependent polarization AP is known very well and given by

$$PA(\lambda) = P\tanh(\mathcal{P}kp\ell\lambda), \tag{6.12}$$

where P is the beam polarization, $\mathcal{P}$ the polarization of the helium, $k = 0.0733$ bar^{-1} Å^{-1} cm^{-1} a constant, p the cell pressure and ℓ the cell length. Unfortunately, the cell transmission decreases while the polarization increases hence the statistics gets very poor where the analyzing power of the cell becomes unity. Nevertheless, it is possible to obtain the absolute beam polarization using the maximum $AP\mathcal{F}$ measurement with the cell because $A = 1$ at this wavelength. This is the opaque region of the spin filter.

Results: We used a ^{3}He-cell with a pressure of 1.4 bar, a length of 10 cm and a nuclear spin polarization of about 50 %. It was positioned in the beam center, replacing the analyzers in figure 6.14. To be insensitive to the spinflip efficiency we polarized the ^{3}He-spins in a way that the neutron beam was blocked when the spinflipper was not working (see e.g. [Rei99]).

Our result is shown in figure 6.19: One can see the polarization increasing with larger wavelength, but at the same time the transmission decreases and the statistics gets worse. However, we can fit a constant to the beginning of the plateau from 7.5 to 9 Å to determine $AP\mathcal{F}_{max}$. Since we know that the analyzing power A is unity at the maximum and that $\mathcal{F} = 1$, we have an absolute measurement of the polarization P in this region.

We made fits to four datasets containing one hour measurements to account for the nuclear spin depolarization. Nevertheless, the maximal value does not change significantly:

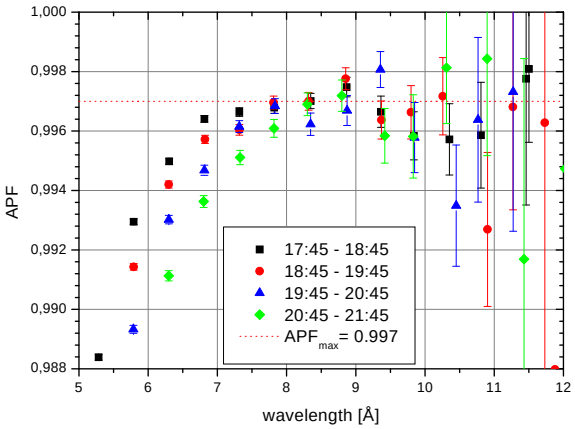

Figure 6.19: $AP\mathcal{F}$ measured with ^{3}He-cells in four different time intervals. The analyzing power A is unity at the maximum, hence we fitted the plateau between 7.5 and 9 Å for all intervals to obtain the beam polarization P ($\mathcal{F}$= 1). The mean value is P= 0.9969 ± 0.0001. We know from figure 6.16 that AP is constant between 2 and 12 Å therefore the beam polarization is 99.7 % in this region.

measurement	fit region	P
17:45 - 18:45	(7.5-9 Å)	$0.9968 \pm 0.0002 \pm 0.0007$
18:45 - 19:45	(7.5-9 Å)	$0.9972 \pm 0.0003 \pm 0.0005$
19:45 - 20:45	(7.5-9 Å)	$0.9966 \pm 0.0002 \pm 0.0008$
20:45 - 21:45	(7.5-9 Å)	$0.9967 \pm 0.0003 \pm 0.0005$

The first error is statistical, the second due to systematic changes in the fit region. Unfortunately it was not possible to perform additional systematic checks because of a lack of time. These checks will be done during the next beamtime, when the polarization analysis will be repeated with increased accuracy at more points in the beam.

The mean value of the four values is $\overline{P} = 0.9969 \pm 0.0003$. Since we determined a flat relative polarization between 2 and 12 Å with the supermirror analyzer method we can conclude that the polarization in this region is P=99.7 % where the statistical accuracy of the measurements is better than 10^{-3}.

We can derive from the difference between the absolute and the relative measurement, which is 0.1 %, that taking the square root of AP in the supermirror method is a quite good approximation. However the polarizers are slightly better than the analyzers.

6.3.3.3 Limitations and Outlook

With a polarization of 99.7 % in the range from 2 to 12 Å we produced the best polarized cold neutron beam so far. However, we can make no quantitative statements for wavelengths λ beyond 12 Å and below 2 Å. The polarization for long wavelengths seems to decrease but statistics is very poor.

Due to the supermirror analyzer cutoff wavelength[4] of 4.5 Å the statistics for $\lambda < 2$ Å is too low to obtain a value for the polarization or the spinflipper efficiency. This may be possible using just one analyzer with increased measuring time or with two long ^{3}He-cells. Generally, this problem is crucial and must be solved because 3.7 % of the neutrons in the $\frac{1}{v}$-spectrum have wavelengths smaller than 2 Å.

The statistics for $\lambda > 12$ Å is limited since this region contains only 2.2 % of the neutrons. It could be improved with longer measurements. However, this is not a critical point for the A measurement since we can easily install a wavelength cutter, which removes neutrons with long wavelengths effectively.

Nevertheless, we can try to make a rough estimation on the overall beam polarization: We measured 99.7 % between 2 and 12 Å. If we assume a polarization $P = 98.5$ % for $\lambda < 2$ Å and $P = 98.0$ % for long wavelengths the result for the mean polarization is $\overline{P} = 99.6$ %.

[4]The cutoff wavelength is determined by the curvature of the supermirrors. It is defined as the smallest wavelength, at which at least 70 % of the incident neutrons can pass the polarizer.

Chapter 7

Summary

The determination of the electron asymmetry A, the correlation between neutron spin and electron momentum, in the decay of free polarized cold neutrons is an excellent method to deduce the element V_{ud} of the CKM quark mixing matrix. A precise value for this element combined with results from high energy physics allows unitarity checks on this matrix.

The aim of this thesis was to improve the experimental setup of the electron spectrometer *PERKEO II* at several points to reduce the uncertainities and corrections in the measurement of the electron asymmetry A with regard to the last experimental run in 1997 [Rei99]:

We designed a new collimation system for the cold neutron beam using Monte Carlo simulations to reduce the beam related background significantly. Compared to the measurement from 1997, we reduced the background from the last diaphragm by 92 %. This was achieved by shifting it away from the scintillators to get a smaller solid angle and by optimizing the size of the diaphragms. At the same time the event rate is only decreased by 9 % due to the smaller diaphragm openings. However, this effect is canceled because we will use the higher neutron flux of the PF1b beamplace at the Institut Laue-Langevin (ILL). Furthermore, we will reduce the background by using diaphragms, which are better shielded with ^{6}LiF, and a beamstop positioned further away from the decay volume.

Provided that no bigger problems arise during the beamtime it should be possible to increase statistics by 50 % with an extended time of data acquisition.

Measurements for the determination of the detector function and to test the detector design were performed in Heidelberg. We can decrease the uncertainity in the detector function using the new YZ-Scanner that was optimized and tested by the author.

Moreover, we changed the data acquisition system from CAMAC to VME whereby we were able to reduce the dead time of the detector system by more than a factor 60. The new data acquisition program `VME-MOPS`, together with the interface `GRAMOPS` and the display program `ROOTMOPS` [Bre03], provides a convenient platform to operate the measurement.

Since the programs work on a normal Linux system, the handling of the large data amounts arising in the measurement is faciliated.

In fall 2003, we performed the first part of the beamtime at the ILL. We installed the beamline and the collimation system in front of the spectrometer and measured the beam polarization: Using two supermirror polarizers in the crossed geometry setup, we obtained a mean polarization $P = 99.7$ % for neutron wavelengths between 2 and 12 Å, where the statistical uncertainity is better than 10^{-3}. The measurements are not sufficient to make a quantitative statement for longer and shorther wavelengths and have to be repeated with an improved setup, nevertheless we can estimate the overall beam polarization to be around $P = 99.6$ %.

We compare the corrections and uncertainities due to beam polarization and spinflipper efficiency[1] of the measurement from 1997 with our new values in the following table:

	correction 1997	uncertainity 1997	correction 2003	uncertainity 2003
polarization	1.1 %	0.3 %	0.4 %	0.03 %
flipper efficiency	0.3 %	0.1 %	0.0 %	0.08 %
sum	1.4 %	0.4 %	0.4 %	0.11 %

The corrections and uncertainities are considerably reduced in the current experimental setup. Combined with the improvements mentioned above it might be possible to see potential deviations from unitarity even in the raw, uncorrected spectra.

[1]Note that the value of the 2003 flipper efficiency is only valid for wavelengths between 2 and 12 Å due to poor statistics for wavelengths above and below. Therefore we have to improve and repeat the measurement to get a value for the whole spectrum.

Bibliography

[Abe97] H. Abele et al., Phys. Lett. B **407**, 212 (1997)

[Abe02] H. Abele et al., Phys. Rev. Lett. **88**, 21 (2002)

[Abe03] H. Abele et al., arXiv:hep-ph/0312150v1

[Abe03b] H. Abele in *Quark-Mixing, CKM-Unitarity*, Mattes Verlag, Heidelberg 2003

[Arn87] M. Arnold, Ph.D. thesis, University of Heidelberg 1987

[Ast97] M. Astruc Hoffmann, diploma thesis, University of Heidelberg 1997

[Bae96] S. Baeßler, Ph.D. thesis, University of Heidelberg 1996

[Bae03] S. Baeßler, private communication

[Baz93] A. N. Bazhenov et al., Nucl. Instr. Meth. **332**, 534 (1993)

[Bre03] M. Brehm, diploma thesis, University of Heidelberg 2003

[Dub03] D. Dubbers in *Quark-Mixing, CKM-Unitarity*, Mattes Verlag, Heidelberg 2003

[Jac57] J. D. Jackson et al., Phys. Rev. **106**, 517 (1957)

[Jac02] J. D. Jackson: *Klassische Elektrodynamik*, de Gruyter, Berlin 2002

[Leo94] W. R. Leo: *Techniques for Nuclear and Particle Physics Experiments*, Springer, Heidelberg 1994

[Lon80] M. A. Lone et al., Nucl. Instr. Meth. **174**, 521 (1980)

[Mae03] B. Märkisch, private communication

[Mar03] W. J. Marciano in *Quark-Mixing, CKM-Unitarity*, Mattes Verlag, Heidelberg 2003

[Mue96] T. Müller, diploma thesis, University of Heidelberg 1996

[Mun00] D. Mund, diploma thesis, University of Heidelberg 2000

[Mun03] D. Mund, private communication

[Nac86] O. Nachtmann: *Elementarteilchenphysik*, Vieweg, Braunschweig 1986

[NDB02] A. Dianoux et al.: *Neutron Data Booklet*, ILL 2002

[Nuc95] G. Pfennig et al.: *Chart of the nuclides*, Forschungszentrum Karlsruhe 1995

[PDG02] K. Hagiwara et al. (Particle Data Group), Phys. Rev. D **66**, 010001 (2002)

[Pet02] A. Petoukhov et al. in *Quark-Mixing, CKM-Unitarity*, Mattes Verlag, Heidelberg 2003

[Plo00] C. Plonka, diploma thesis, University of Heidelberg 2000

[Pov01] B. Povh: *Teilchen und Kerne*, Springer, Heidelberg 2001

[Rav95] C. Raven, diploma thesis, University of Heidelberg 1995

[Rei99] J. Reich, Ph.D. thesis, University of Heidelberg 1999

[Sch89] O. Schärpf, N. Stuesser, Nucl. Instr. Meth. **248** (1989)

[Sch95] P. Schmüser: *Feynman Graphen und Eichtheorien für Experimentalphysiker*, Springer, Heidelberg 1995

[Ser98] A. Serebrov et al., JETP **86**, 1074 (1998)

[Sib01] K. Sibold: *Therie der Elementarteilchen*, Teubner, Stuttgart 2001

[Sol02] T. Soldner, A. Petoukhov, C. Plonka: *Installation and first tests of the new PF1b polarizer*, ILL Internal Report ILL03SO10T (2002)

[Sol03] T. Soldner, private communication

[Wu57] C. S. Wu et al., Physical Review **105**, 1413 (1957)

[Zim99] O. Zimmer, Phys. Lett. B **461**, 307 (1999)